THESIS

THE ROLE OF FAULTS AND VOLCANO-TECTONIC EVENT IN TOXIC GASES EMISSIONS IN DIENG VOLCANO AND ITS DETECTION IN ASTER TIR IMAGERY

This submission to the Double Degree M.Sc programme, Gadjah Mada University and International Institute for Geo-Information Science and Earth Observation in partial fulfillment of the requirement for the degree of Master of Science in Geo-Information for Spatial Planning and Risk Management

By :
Kusnadi
UGM : 13/357419/PMU/08060
ITC : s6013651

Supervisors :

1. **Prof. Dr.rer.nat. Junun Sartohadi, M.Sc (UGM)**
2. **Dr. Chris Hecker (ITC)**

DOUBLE DEGREE M.Sc. PROGRAMME
GADJAH MADA UNIVERSITY
FACULTY OF GEO-INFORMATION SCIENCE and EARTH OBSERVATION
UNIVERSITY OF TWENTE
2015

DISCLAIMER

This document describes work undertaken as part of a programme of study at the Graduate School, Gadjah Mada University and Faculty of Geo-Information Science and Earth Observation, University of Twente. All views and opinions expressed therein remain the sole responsibility of the author, and do not necessarily represent those of the institutes.

Yogyakarta, April 2015.

Kusnadi

ABSTRACT

Dieng volcano is a complex volcanic system which is located in Central Java, Indonesia. It has several craters that release toxic gases which the mechanism of toxic gases outburst remains unknown. The spatial temporal analysis of seismic features and CO_2 emissions rate which is based on fault analysis and time series analysis can reveal an understanding about the control mechanism of toxic gases outburst event. The fault analysis which used manual and automatic lineaments extraction method successfully characterized the correlation between faults and the distribution of craters. Small and narrow craters in West part of Dieng area are correlated with complex fault system where most of toxic gases outburst events occur in this area. Meanwhile, large craters in East part area are in line with single fault system where fewer events of toxic gases outburst occur in the area. These findings are also supported by most of local tectonic and VTA earthquakes. The time series of seismic and CO_2 emissions rate are employed to know the periodical behavior and correlation between seismic events and volcanic unrest activities. The cyclical pattern analysis of time series data showed that the toxic gases outbursts events have no correlation with the cyclical period of local tectonic and VT earthquakes. The cross correlation analysis of long-term seismic events shows that strong local tectonic earthquakes and high frequency of seismic events has a correlation with the events of toxic gases outbursts. Meanwhile, a phreatic eruption in 2009 has no correlation with the seismic events. This cross-correlation analysis of long-term seismic events also supports the fault analysis. Meanwhile, the cross correlation analysis of short-term seismic events and toxic gases outburst event in 2011 represents the delay times and inverses relationship between seismic events and toxic gases outburst event. This study also tried to explore the use of spaceborne remote sensing in monitoring volcanic activities in Dieng volcano. Two potential monitoring approaches such as SO_2 gas and temperature anomaly changes were retrieved from ASTER TIR images. The SO_2 gas plumes were not captured in the ASTER TIR images. The temperature anomaly analysis is good to identify the difference between the surface temperature of the crater and the surface temperature of its surroundings. It is believed that the ASTER TIR can be a useful monitoring tool if ASTER TIR images can show the difference of the temperatures. In this study, the monitoring of temperature anomaly can be proceeded for Sileri crater when the seismic monitoring fails to detect the event of phreatic eruption.

Keywoords: *Dieng volcano, fault analysis, cyclical pattern analysis, cross correlation analysis, ASTER TIR, SO_2 retrieval, and temperature anomaly extraction.*

ACKNOWLEDGEMENT

I praise to ALLAH SWT who gives grace and health to finish this work.

I am deeply grateful to my supervisors, Prof. Dr. Junun Sartohadi and Dr. Chris Hecker for the chance to work with them, for the guidance, for the patience and for the immense in leading me to finish my thesis.

I give special thanks to Dr. David Rossiter for his time to discuss about statistic time series analysis, to Dr. Robin Campion for sharing knowledge about SO_2 retrieval, to ASTER team for providing the ASTER scenes of Dieng volcano, to PVMBG who allowed me to use the seismic and gases data of Dieng Volcano, to Aziz Yuliawan and Surip who provided me the seismic and CO_2 data of Dieng volcano and also for their guidance during the fieldwork activity, to Sarwanto who allowed me to stay in the mes of observatory office of Dieng volcano during my fieldwork time.

I also give gratefully thanks to UGM course coordinator Prof. Sudibyakto, MS and ITC coordinator Mr Bart Korl and Mr Harald van der Werf who arranged this course very well and provide helps and supports to us.

I also give special thanks to my colleagues Febri Syahli, Astisiasari, Dwiyanti Kusumaningrum and Radius Ramli for help me in improving the English writing of my thesis.

I thanks to Bappenas and Stuned NESO Scholarships who gave me opportunity to study in UGM, Indonesia and ITC, The Netherlands. I would not be able to reach my M.Sc title without their supports.

I thank to all UGM and ITC lecturers who provided me with great knowledge and staffs who helped me with the administration stuff during the 2 years of study, to all of my friends in UGM and ITC who gave unforgettable and very fascinating moments and always provided helps during this 2 year of study.

Finally, I also thanks to my family who always gave supports and prayers for me in finishing my study.

TABLE OF CONTENTS

LIST OF FIGURES

LIST OF TABLES

Chapter 1. Introduction

This chapter describes the background of the research, problem statement, research objectives, research questions, and scientific significance.

1.1 Background

Indonesian archipelago as part of the ring of fire has 129 active volcanoes (Abidin et al. 2007). Most of the active volcanoes are explosive due to the subduction of three major plate tectonics; Indo-Australian, Eurasian and Pacific (Katili 1974). In the western and central parts of Indonesia (Sumatra, Java and Nusa Tenggara), the Indo-Australian plate subducts beneath the Eurasian plate with the motion from 63 mm/yr N14° at Sunda strait to 70 mm/yr N13° at south of Bali and Nusa Tenggara (Pacey et al. 2013). The motion generates a pressure between the surfaces of each plate and it causes rocks to melt and fill the magma chamber. Subsequently, the increased volume and pressure of the magma chamber cause the eruption which can create hazardous effects. The typical hazards that can occur are pyroclastic flow, pyroclastic surge, ash fall and lahar (Jousset & Pallister 2013).

However, toxic gas hazard has a slight different process. It usually occurs in volcano within hydrothermal system (Barry et al. 2014). This type of volcanoes is a second order volcano, which forms after a forming of large caldera. It is characterized by deep heat flux of the magma chamber (Giggenbach et al. 1991). The magmatic process takes insignificant role in the volcanic activity in the shallow to the surface of the earth. Therefore, the eruption type in this type of volcanoes is dominated by a phreatic eruption which is triggered by the hydrothermal energy.

Dieng volcano is a volcano with hydrothermal system. It is situated on a large plateau which has high potential for farming activity. This condition attracts people to stay close to the volcano. Based on that fact, the effect of volcanic eruption (phreatic eruption and toxic gases) is covering a local area, Dieng volcano becomes a hazardous volcano. The occurence of the toxic gases outburst

events have been reported several times since the 1825. The worst event was in the 1979 which killed 149 people in the Kepucukan village of Dieng (Geological Agency of Indonesia n.d.). The series of toxic gases outburst events show the occurance of the local tectonic earthquake. Thus, volcanic activity may not be the only trigger of the toxic gases outbursts in Dieng volcano. Tectonic activities in the local area may play an important role, as well.

The government of Indonesia through the Volcanology and Geological Hazard Mitigation Center (PVMBG) has been established the monitoring of Dieng volcano using geophysical and multi-gases detection tools (Geological Agency of Indonesia n.d.). The geophysical equipment (seismograph) measures the seismic event in the Dieng volcano; while, the multi-gases detection tools measure the gases content in two craters of Sileri and Timbang. Time series data of the area collected by these tools would then provide valuable information to understand the processes that affect the eruptions sequences in Dieng volcano.

In the term of monitoring, advancement of remote sensing provides valueable information in detecting several features of volcano (Ramsey & Harris 2013). Toxic gases are the main features in Dieng volcano (Guern et al. 1982) released below health threshold in normal conditions (<2% mol. for CO_2) and above health threshold in toxic gases outburst events. Normal condition of toxic gases emissions in daily basis has a probability to be extracted from remote sensing (Campion et al. 2010). The easiest gas to detect is sulfur dioxide (SO_2) (Urai 2004) as it is strongly absorbent of thermal infrared radiation. Furthermore, SO_2 gas is mainly produced by volcanoes. Therefore the confusion with gases from non-volcanic sources during data acquisition related to their concentration in the atmosphere is less problematic. It can be extracted from the region of Thermal infrared (TIR) and ultraviolet (UV). Another feature is temperature changing within the craters. An extreme temperature changing in fumaroles during an eruption phase is reported to have a correlation with the increasing of geophysical and geochemical signal (Spampinato et al. 2011).

However, there are some challenges in measuring SO_2 fluxes in a volcano with distributed craters such as Dieng Volcano because SO_2 gas is not

only released from one crater and its concentrations are varies between craters. Furthermore, The solar heating effect can also interfere the quantification of true background temperature on the craters of Dieng volcano, because the temperature value on the surface of craters is far below the magmatic value (Vaughan et al. 2012).

One potential remote sensings imageries to be used in the Dieng volcano is the Advanced Spaceborne Thermal Emission and Reflection Radiometer (ASTER). High resolution of the ASTER TIR region has capability to acquire the SO_2 flux as well as the thermal information on land and water surface (Campion et al. 2010; Yamaguchi et al. 1998).

1.2 Problem statement

Previous studies for toxic gases in Dieng volcano were concerned on the origin and the composition of gases (Allard et al. 1989; Guern et al. 1982). A study about the mechanism controling the toxic gases outburst events has not been conducted yet. The volcanic toxic gases outburst events have a possibility to correlate with the volcanic and tectonic process underneath the Dieng volcano. The volcanic and tectonic process are usually represented by the seismic activity such as volcano tectonic (VT) and local tectonic earthquakes and surface manifestation such as fault. Therefore, a study about spatial and temporal correlation between seismic features (local tectonic earthquake and the VT events) and the gases emission could bring an understanding of a specific mechanism that control the volcanic unrest activities such as phreatic eruption and toxic gases outburst event in Dieng volcano.

Furthermore, Dieng volcano is a complex volcanic system manifested by a number of craters. Most of the craters have hazardous effect to the community. Thus, they need an intensive monitoring. However, it is difficult to monitor separated craters using conventional ground based approachs. Remote sensing approach sounds more promising as a complement equipment to monitor the toxic gases emissions in Dieng volcano. Remote sensing approach meets the criteria of low cost, large coverage, rapid and real time detection (Urai 2004) for monitoring

the toxic gases outburst events in Dieng volcano. However, in the case of Dieng volcano with many small craters, the effectiveness of monitoring using remote sensing needs to be assessed.

This research analyzes the spatial and temporal correlation between fault zone, local tectonic, and VT toward toxic gases emissions by implementing fault analysis and time-series statistical approach. Moreover, the capability of the multi-temporal TIR bands of ASTER to measure the SO_2 flux from passive degassing event as well as to identify the normal background temperature would bring a further understanding to the remotely-sensed measurement using ASTER TIR images; especially the craters and the fractures zones in Dieng volcano.

1.3 Research Objectives

The main objective of this research is to assess the role of fault (fault zone and local tectonic earthquake) and volcano-tectonic events in the toxic gases emissions in Dieng volcano. Moreover, it also to detect the toxic gases anomaly by using ASTER TIR images. The detail objectives are:

1. To find the correlation between fault system and craters distribution.
2. To analyze the cyclical pattern of seismic features data
3. To find the correlation between seismic features and toxic gases outburst events.
4. To retrieve the sulfure dioxide (SO_2) from ASTER TIR.
5. To detect the normal background temperature anomaly of craters and fractures zone by using ASTER TIR images

1.4 Research Questions

There are some research questions that are needed to be addressed in order to achieve the research objectives:

1. How can we detect the fault?
2. What is the correlation between fault and craters distribution?
3. How can we calculate the cyclical pattern of seismic features?
4. Are the cyclical patterns same among seismic features?
5. What are the correlation between cyclical patterns of seismic features and toxic gases outburst events in Dieng?

6. What are the correlations between seismic features and toxic gases outburst events in Dieng?
7. Can we detect the gas plume from Remote Sensing in the Dieng volcano context?
8. How can we retrieve the SO_2 fluxes from TIR images?
9. How is the relation between SO_2 emission from ground data and spaceborn data?
10. How can we detect temperature anomaly from ASTER TIR?
11. Are there any correlation between temperature anomaly with the craters and the fractures zones?
12. What are the normal background temperatures in each craters and fractures zones?

1.5 Scientific significance

The main significance of this research is the understanding of the relations between fault and VT with the toxic gases in complex system of Dieng volcano. Dieng volcano is a good example of a volcano with complex system. Hydrothermal and tectonic cause the features in the system. This research is important to improve knowledge about the process within a volcano and its manifestation on the surface. And also gives understanding about its effect from different process such as tectonic to the volcanic activity especially in the releasing of toxic gases and phreatic eruption. In the context of monitoring, it enriches knowledge of people who conduct the Dieng volcano monitoring or other similar types of volcano and how to predict the volcanic event based on its correlation with fault and VT.

Furthermore, application of ASTER for SO_2 flux and temperature extraction can provide deeper understanding about the use of ASTER. ASTER with 90x90 meter spatial resolution can detect the SO_2 gases from the normal degassing events in Dieng volcano and the temperature anomaly in the surroundings of the craters and fractures areas. The use of ASTER is important to improve monitoring procedures in Dieng volcano.

Chapter 2. Literature Review

Literature review provides the theoretical background of this research including the concept of volcanic gases hazard, fault lineament, monitoring of volcanic gases, analysis of volcanic time series data, thermal infrared remote sensing, ASTER, SO_2 retrieval, surface temperature anomaly, and temperature correction.

2.1 Characteristic of Volcanic Gases Hazard

Volcanic gases are released by volcanoes during the eruption and/or during their dormant phase. In general, based on their toxic effects, volcanic gases are divided into two categories: asphyxiant and irritant (Baxter & Kapila 1989). Asphyxiant gases disturb the distribution of oxygen, while irritant gases directly irritate the lung tissue, mucous and skin.

The main asphyxiant gas of volcanoes is CO_2. A characteristic of CO_2 is that it is denser than air. Therefore, it accumulates on the ground. The highest concentration of CO_2 gas emission usually occurs in volcanic terrain within hydrothermal systems (Barry et al. 2014). The deep heat flux of the magma chamber produces CO_2 that travels and accumulates at the shallow level (Giggenbach et al. 1991). An earthquake and phreatic eruption can act as the agent for releasing CO_2 to the surface. The morphology of volcano also plays an important role in the accumulation of the destructive volume of the CO_2. There are two types of volcanoes that can generate high CO_2 concentration. The first is Lake Nyos Type. The Lake Nyos type is characterized by a deep crater-lake and fumaroles with low temperatures below 300^oC (Giggenbach et al. 1991). The second type is usually owned by volcanoes in Indonesia like Dieng and Papandayan. This type has a characteristic feature of volcano-tectonic depressions or eroded calderas. In cases of Dieng volcano earthquake and phreatic eruption could trigger gases releasing in large quantities.

SO_2 is one of the main irritant gases after HCl. It is less dangerous than CO_2. The irritant effects cause difficulty in breathing, coughing, tightness in the

chest, soreness of nose, and pain in throat and eyes. Therefore, high concentration of SO_2 is easy to be detected. In addition, SO_2 takes long time (24-36 hours) to kill people.

Previous work indicates that SO_2 can be used for forcasting volcanic events (Werner et al. 2013; Olmos et al. 2007). SO_2 is produced from magma at depth between 4-5 km within the volcano (Bruno et al. 2001). Hence, the increased SO_2 volume at the surface could indicate increasing activity of a volcano at depth.

2.2 Fault Lineament

In most volcanoes, local tectonic activity has no effect to volcanic eruption. However, it can be a main cause for several volcanoes with hydrothermal system such as Dieng volcano to line up (Allard et al. 1989).

A manifestation of tectonic activity is an active fault. On the surface, fault can be represented by a linear or curved line depresion (Jordan & Schott 2005). Their shape can be extracted as lineament in the topographic map or remote sensing images. Lineament is a linear or curved line edge in a landscape which represents an underlying geological structure (Soto-pinto et al. 2013), such as fault, fold and joint. Lineament interpretations mostly use topographic and remote sensing images. The advance in GIS and remote sensing provide fault lineament analysis in cost effective ways. The fault lineament analysis can be done by two main approaches: manual and automatic (Hashim et al. 2013).

The manual extraction mostly depend on the expertise which is supported by a good visualization of image. Combination between DEM image and remote sensing image could provide better visualization of the map especially to enhance the appearance of fault lineament. Automatic process would extract lineament from tonal contrast or assertive edge to patterns, textures and reliefes in the image. The type of input data is very crucial to the result of the extraction (Hashim et al. 2013). Dense vegetation coverage for tropical area often mixes the fault lineament with vegetation boundery and man-made features when utilize an optical remote sensing image. Therefore, the most appropriate source for automatic lineament

extraction in tropical area is digital elevation model (DEM) image. The advantageous of the automatic process is it can extract very small to large scale of lineaments, which can be used for trend analysis of the dominant direction of the lineament. The manual and automatic process can be a good combination for better understanding of the main fault lineament, its type, and the force direction.

2.3 Monitoring of Volcanic Toxic Gases Hazard

Monitoring of volcano helps scientists to assess hazard types and its magnitudes. It can be done by using three main methods (Www.usgs.gov & IRIS n.d.). The first is ground deformation monitored by GPS and tiltmeter. The second is volcano-tectonic features observed by local seismological networks. And the third is gas monitoring by using aerial reconnaisance and land based tools. Another monitoring procedure is a visual monitoring (Abidin et al. 2007). Hydrology monitoring is a complement in the monitoring of volcanic activity.

Monitoring of volcanoes with toxic gases hazard has the same way with the other volcanic hazards. However, in the case of Dieng ground deformation monitoring is less helpful (Abidin et al. 2007). The main hazards in Dieng volcano, toxic gases and phreatic eruptions, do not affect the volcano's morphology when it erupted.

2.3.1 Seismic Monitoring

Movement of magma or other fluids through conduit forces the host rock to break or crack and to vibrate (Zlotnicki et al. 2000). High-magnitude of earthquake will be generated when rocks break. While, low-magnitude of earthquakes or volcanic tremors are driven from cracks vibrations.

Seismic monitoring uses seismometer to aquire seismic data. It is concisted of two main components: seismometer to record the seismic signal within volcano and seismograph as the receiver (Figure 2.1). The blue part is a set of tools, mounted on the field which measures the seismic signals from volcano. The green part is a set of tools, installed in observatory office which main utility is to read the signals sent from the seismometer.

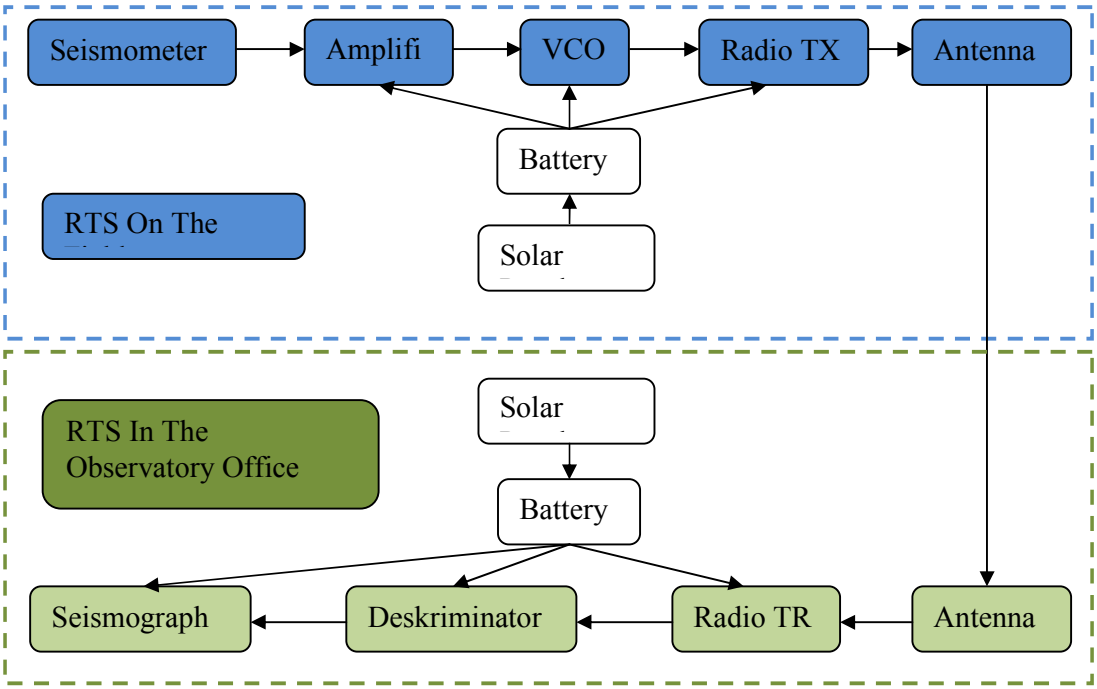

Source : Observatory office of Dieng Volcano

Figure 2.1. Local seismological network scheme using radio telemetric system (RTS). VCO is a Voltage-Contolled Oscillator, radio TX is transmitter and radio TR is transceiver/receiver.

The seismic monitoring tool can provide additional discrimination of tectonic as well as VT earthquake subtypes. The example of tectonic earthquake is tectonic and local tectonic earthquake. The difference between tectonic and local tectonic earthquake is : tectonic is affected by the tectonic activity outside the volcano range while local tectonic earthquake is usually triggered by local tectonic activity. The VT earthquake consists of deep VT (VTA), shallow VT (VTB), tremor, gas burst, and low frequency (LF). It is categorized based on the relative depth to the surface of volcano and the characterisitc and magnitude of eathquake (Zlotnicki et al. 2000) . The deep, high-magnitude earthquake, VTA is in the depth with range of 2 to 5 km from the summit, while the shallow, high-magnitude earthquake, VTB is above the VTA. The tremor, gas burst and low frequency are low-magnitude earthquake which are located nearby the volvano's

surface. In the context of volcanic unrest activity, VT earthquakes are series events started by the increasing of VTA earthquake and followed by VTB, tremor, gas burst and low-frequency earthquake respectively.

In the case of Dieng volcano with the toxic gases and phreatic eruption hazards, the tremor, gas burst and low-frequency earthquake have very low-magnitude which are mostly undetectable in the ground. Their earthquakes some time can be detected during the toxic gases outbursts (Surip, a volcanology officer in Dieng volcano).

2.3.2 Gas monitoring

Gases emission can be measured using several tools and methods such as the correlation spectrometer (COSPEC), Fourier transform infrared spectrometer (FTIR) and MultiGAS (specifically for Dieng).

COSPEC is a sensor to measure the amount of ultraviolet light absorbed by SO_2 molecules within a volcanic plume (USGS n.d.). It is used only for monitoring SO_2 emission. Calibration of the instrument is conducted by contrasting all measurement to an accepted SO_2 standard installed in the instrument. The COSPEC can be installed in a vehicle, on a tripod, and in an aircraft to scan a plume (Figure 2.2). However, the COSPEC that mounted in an aircraft acquires the most precision results (USGS n.d.) because aircraft flies underneath and through the direction of traveled plume.

Source : http://volcanoes.usgs.gov/activity/methods/gas/plumes.php

Figure 2.2. Cospec from the plane (a), from the vehicle (b) and from a stationary tripod (c).

The FTIR is an infrared based camera for measuring volcanic gases (USGS n.d.). The open-path and closed-path system provide capability for

measuring gases simultaneously (Figure 2.3). The optical telescope is used by open-path method to capture a target gas in away distance. The closed-path method has a contrast function. The gases from a plume or fumarole are sucked into a container, driven by car to the lab and then measured with a lab FTIR that is equipped with a gas cell.

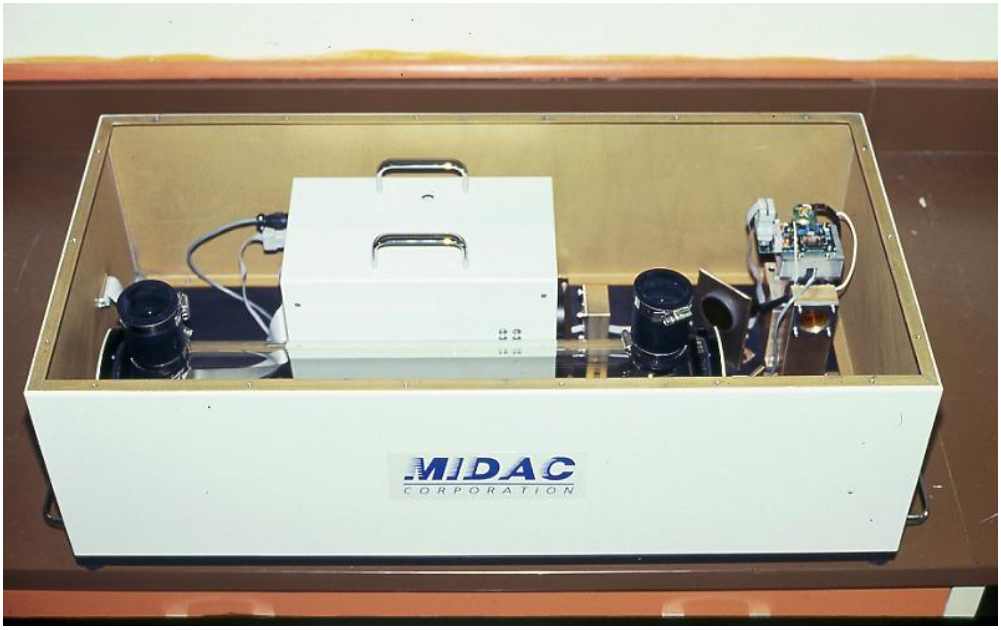

Source : http://volcanoes.usgs.gov/activity/methods/gas/plumes.php

Figure 2.3. Interior view of a closed-path FTIR. It shows gas cell, Michelson interferometer, globar light source, helium-neon laser, and MCT detector.

MultiGAS is an experimental monitoring for volcanic gases. It is a realization of the bilateral cooperation between Indonesian goverment (PVMBG) and United State Geological Survey (USGS). It works by inhale the gases from the crater and detects the gases concentration by three sensors, installed in the tools (SO_2, CO_2 and H_2S) (Figure 2.4). Previously, the Investigation and Technological Development of Geological Disaster Board (BPPTKG) builds a single gas reader for monitoring the CO_2 emission rate in Timbang crater. Its data acquisition has the same method with the MultiGAS reader.

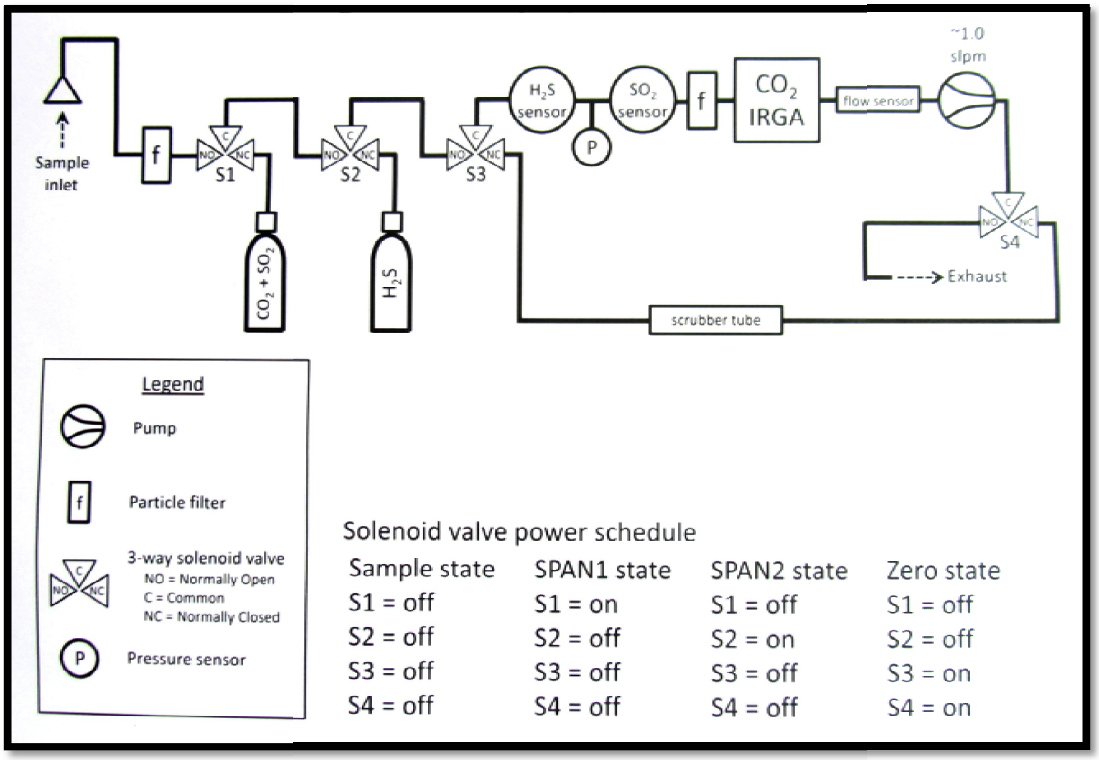

Source : Observatory office of Dieng Volcano
Figure 2.4. Sileri MultiGAS (CO_2, SO_2, and H_2S) pneumatic layouts

2.4 Analysis of Volcanic Time Series Data

Time series data analysis aim to understand the past trends and to predict the possible future events, enabling managers or policy makers to make properly informed decisions (Cowpertwait & Metcalfe 2011). Time-series data analysis has four characteristics that distinguish them from the non-temporal variables analysis (Rossiter 2012):

- The variable may shows a trend over time;
- The variable may perform some cycles of different period;
- The subsequent observations always have serial correlation;
- The"white noise" is almost always shown by the variable i.e. did not explain a random variation by any of the above.

In the case of volcanoes, time-series analysis proposes a robust method of characterising long-term behaviour within geophysical systems (Lamb et al. 2014). It also offers the automated identification of 'thresholds', or changes in the patterns of behaviour for the long-term monitoring of active volcanoes. Basic characteristic of volcanic time series data is non-linear, therefore, volcano time series analysis is more focus in the analysis of cyclical behaviour rather than in trend pattern (Nicholson et al. 2013).

Three common methods to analysis the cyclical pattern of time series are fast fourier transform (FFT), detrended fluctuation analysis (DFA) and probabilistic distiribution analysis (PDA). FFT is a method for decomposing dominan cycle period of time series (Nicholson et al. 2013). It works by transforming a function of time into a function of frequency (Chen & Chen 2014). It is the most robust method for calculating non-stationary time series with no priori cycle (Lamb et al. 2014). DFA is a mathematical method for specifying the statistical self-affinity of a signal (Peng et al. 1994). It can avoid an artifact when analyzing a long-range nature correlation of time series data. PDA is a stochastic time series analysis by fitting the statistical distribution of time series data. Using log-logistic model to estimate probabilistic value of variables. (Lamb et al. 2014)

On the other hand, volcanic eruption can be forcasted by analyzing several signals (tectonic local, volcano-tectonic, and gases emission) that rise during the pre-eruptive event. The signals can be a continues process, where one signal can be followed by another signal (Budi-santoso et al. 2013). Therefore, it is important to know the correlation between volcanic signals for better undestanding toward the characteristic of volcanic eruption event.

Time series data of several signals can also be analyzed to know the correlation between the signals (Nicholson et al. 2013). The unique feature of time series correlation is that the correlation depending not only on the value of correlation but also on the lag (time different) (Rossiter 2012). The correlation can be a serial, where the highest correlation value is not always occur in the lag 0 (same time). The lag distance can be a consideration for the correlation level,

where too far lag can be consideredas uncorrelated, even though the correlation value is high.

2.5 The Advanced Spaceborne Thermal Emission and Reflection Radiometer (ASTER)

The Advanced Spaceborne Thermal Emission and Reflection Radiometer (ASTER) is a high spatial resolution multispectral imager which is provided by the Ministry of International Trade and Industry (MITI), Tokyo, Japan, launched in December 1999 (Yamaguchi et al. 1998). It has three subsystems; the visible and near infrared (VNIR), the short-wave infrared (SWIR), and the thermal infrared. The VNIR subsystem as a name produces three spectral bands at wavelengths between 0.52 – 0.86 μm, with a spatial resolution of 15 m. It is equipped by two telescopes: one nadir-looking with a three-spectral-band detector, and the other is a backward-looking with a single-band detector. The SWIR subsystem that has six spectral bands in the wavelengths between 1.60 – 2.43 μm using a single, nadir-pointing telescope with a spatial resolution of 30 m. The ASTER/TIR subsystem is operated in five spectral bands (bands 10–14) through a single, fixed-position, nadir-looking telescope that provides 90 m resolution. These bands can be used to retrieve surface temperature and surface spectral emissivity. These potential capability drives ASTER to be used in a wide variety of studies such as geological mapping, environmental monitoring, and hazard prediction. Table 2.1 shows a detail instrument classification of the ASTER subsystem.

In the field of volcano, the Thermal Infrared (TIR) region has the capability to provide land surface temperature (LST) and volcanic gases concentration (VGC) data by retrieving the spectral attenuation of infrared terrestrial radiation (Carlos et al. 2008; Ramsey & Dehn 2004), that capability is supported by the advances in airborne and spaceborne sensors (Vaughan et al. 2005) and in analytical techniques including the development of algorithms that can extract additional information from the pixel (Vaughan et al. 2010).

In order to calculate VGC and LST, high resolution of TIR images (90-m spatial resolution) and less disturbance wavelength (8.1 to 11.6 μm) of ASTER are used in order to calculate VGC and LST(Yamaguchi et al. 1998). ASTER TIR image is proven to be successful in retrieving VGC and LST (Urai 2004; Gillespie et al. 1998).

Table 2.1. ASTER instrument specifications (after (Pieri & Abrams 2004)

Characteristic	VNIR	SWIR	TIR
Spectral range	Band 1: 0.52 – 0.60 μm, Nadir looking Band 2: 0.63 – 0.69 μm, Nadir looking Band 3: 0.76 – 0.86 μm, Nadir looking	Band 4: 1.600 – 1.700 μm Band 5: 2.145 – 2.185 μm Band 6: 2.185 – 2.225 μm Band 7: 2.235 – 2.285 μm Band 8: 2.295 – 2.365 μm Band 9: 2.360 – 2.430 μm	Band 10: 8.125 – 8.475 μm Band 11: 8.475 – 8.825 μm Band 12: 8.925 – 9.275 μm Band 13: 10.25 – 10.95 μm Band 14: 10.95 – 11.65 μm
Ground resolution	15 m	30 m	90 m
Data rate (Mbits/s)	62	23	4.2
Cross-track pointing (^{o})	$\pm$24	$\pm$ 8.55	$\pm$ 8.55
Cross-track pointing (km)	$\pm$318	$\pm$ 116	$\pm$116
Swath width (km)	60	60	60
Detector type	Si	PtSi – Si	HgCdTe
Quantization (bits)	8	8	12

2.5.1 SO_2 Retrieval

The SO_2 retrieval depends on the wavelength of absorption features (Watson et al. 2004). SO_2 from volcanic plume absorbs and emits a certain

wavelengths of electromagnetic radiation. The most affected wavelength is at 8.7 μm. It is signed by reducing radiance reaching the salellite at the wavelength (Figure 2.5.a), which is correlated with the band 11 of ASTER. Thus, the focus of SO_2 retrieval would be on the affected bands. The calculation of SO_2 column abundance uses a technique developed by (Realmuto & Worden 2000) which is based on the sensor reaching radiance coeficiant as follows:

$$Ls = \{\varepsilon_g B(T_g) + (1 - \varepsilon_g) L_d/\pi\} t_a + L_u \quad (1)$$

Whereas;
Ls : At sensor radiance
$\mathcal{E}_g$: Emissivity of the ground
B : Planck function
T_g : Ground temperature
L_d : Downwelling radiance (ambient, sky radiance at the ground)
t_a : Transmission of the atmosphere
L_u : Upwelling radiance (ambient, sky radiance at sensor)

Other researcheres add an improvement and modification in input parameters. For example, Campion et al. (2010) prefers to use band ratios (B10+B12)/2*B11 and B14/B11 as SO_2 affected band input rather than single B11 of ASTER TIR images to avoid the effects of surface temperature and altitude, plume temperature and atmospheric humidity. The temperature parameter is extracted from ASTER TIR using different methods, depend on the situation of volcano. The temperature emissivity separation (TES) method is good for examining the land surface temperature (LST) while the split window algoritm is fit for volcano island wich is surronded by water (Gillespie et al. 1998). MODTRAN radiative transfer codes are used to drive the local atmospheric condition such as upwelling and downwelling radiances and the transmission of a user-defined atmosphere. The SO_2 flux is then obtained from the calculation of SO_2 column abundance with wind velocity and plume profile. For ASTER image, Davies et al. (2007) uses three different angles images from the Multiangle Imaging Spectroradiometer (MISR) to generate wind speed and plume height. However, the rough spatial resolution of MISR affect erroneous in height between 300-400 m. In addition, Urai (2004) develops a technique to generate

wind velocity direct from two images of ASTER nadir and backward looking image which is more efisient in data usage and it has higher spatial resolution.

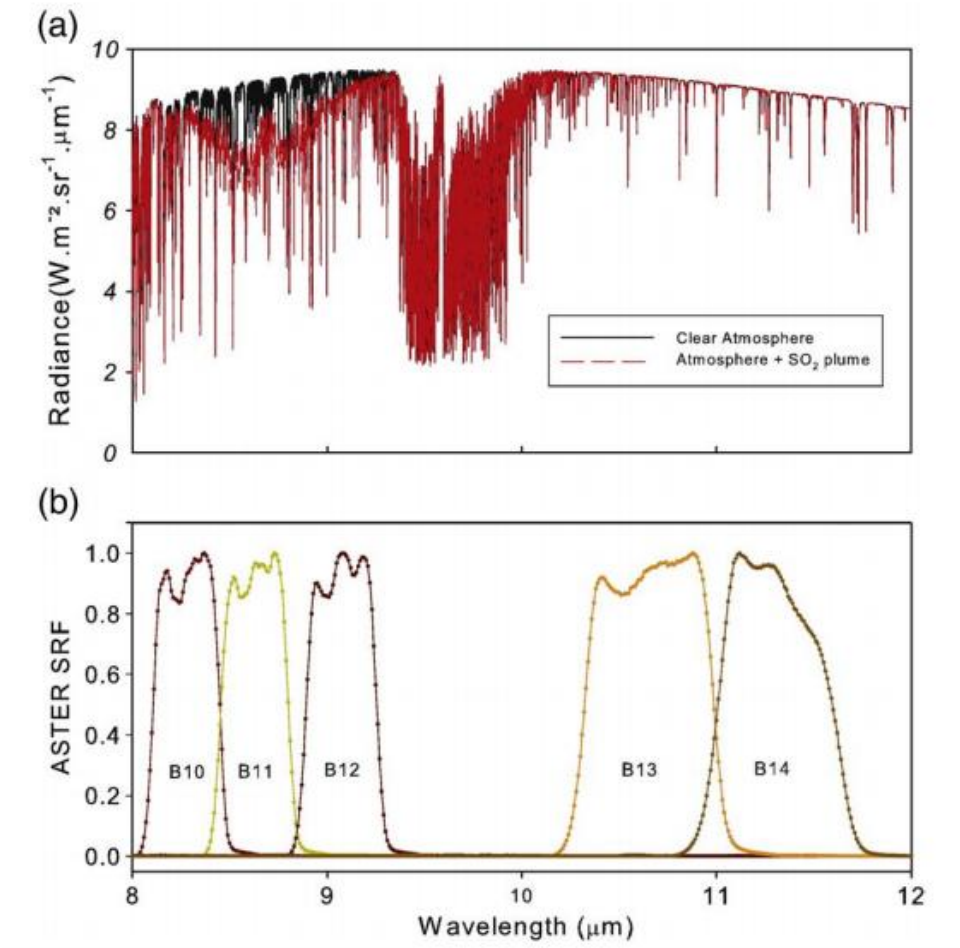

Figure 2.5. The diagram of ASTER TIR atmosphere radiance per wavelength. (a) The spectral radiance of a "clean" atmosphere (black) and an atmosphere containing 10 g/m² of SO_2 (red dashed). (b) Normalized Spectral Response Function (after (Campion et al. 2010).

Good accuracy of retrieved SO_2 parameters will affect the result of SO_2 flux. The use of band ratio (B10+B12)/*11 and B14/B11, temperature extraction by TES method, local atmoshperic condition from MODTRANT radiative tranfer codes, and the wind velocity generated from ASTER nadir and backward looking image can provide a better SO_2 flux result for Dieng volcano.

2.5.2 Surface Temperature Anomaly from ASTER TIR image

Surface temperature anomaly is a feature in volcanic eruption that can be detected using TIR remote sensing (Carter et al. 2008). The feature would show a contrast temperature compared to the surronding area which is manifest the temperature of fumaroles. However, the true temperature of the fumaroles can not be manifested exactly due to the spatial resolution of the image (Lagios et al. 2007). Therefore, the background temperatures must be determined to allow the monitoring of the significant changing in the temperature of fumaroles related to the eruption phase.

ASTER TIR image is the highest spectral resolution of TIR image which is aviliable for the Dieng volcano. Multispectral ASTER TIR can accomadate any variety of surface through the wavelenghts for better distinguished of volcanic features from surronding area and determined the surface background temperature of volcanic features (Coll et al. 2007). As the SO_2 retrieval, the temperature extraction is also based on the at-sensor radiance of ASTER. Where, the square bracket in the Eq. 1 calculates the at-ground radiance (L_g). L_g can be formulated if the atmosphere transmission (t_a) and upwelling radiance (L_u) are known from the equation below:

$$L_g = \frac{L_s - L_u}{t_a} \qquad (2)$$

There are two main methods to extract temperature from ASTER TIR scenes. Temperature emissivity separation (TES) is one of algortihm, built to extract the temperature and emissivity from TIR region (Gillespie et al. 1998). TES is widely used and validated for calculating the temperature especially land surface tempertature (LST) (Gillespie et al. 1998; Cheng et al. 2008; Jacob et al. 2004; Gillespie et al. 2011; Sabol, Jr. et al. 2009). It calculates the Tg and ε_g as a couple. Another algorithm is the split window algorithm. This algorithm uses two or more bands by exploring their differential atmospheric absorptions. It assumes that there is a correlation between the difference in radiance measured in the two bands and the amount of the attenuation (Carlos et al. 2008). It is powerfull for examining water surface temperature. Trunk & Bernard, (2008)use split window

algorithm to investigate crater lake temperatures in four volcanoes; Ruapehu, Poás, Kawah Ijen, and Copahué using ASTER TIR scenes. For LST, bare surface can affect to mix result (Gillespie et al. 1998) caused by unknown emissivity differences between bands.

2.5.3 Temperature Correction

The study area is a mountain region which has a terrain with undulating to steep slope. In the term of TIR remote sensing, this condition can affect lapse rate and illumination effect. The lapse rate is a spatial and temporal negative change of actual temperature due to altitude (dT/dz) (Evrendilek et al. 2012). It can be arranged from altitude image by applying simple linear regression procedure. While, the illumination affects the absorption of solar radiation. It rely on the relative orientation of the pixel against the actual position of the sun. The illumination effects can be corrected by the aspect and the slope, which also applying the regression procedure. Ulusoy et al. (2012) has successfully applied this three parameters to improve temperature anomalies in the hot spots and hydrothermal areas of Mt. Namrut volcano in Turkey.

Chapter 3. Study Area

This chapter shows an overview of Dieng volcano and Summary of Dieng volcano activities.

3.1. An Overview of Dieng Volcano

The research is conducted in Dieng located in six districts of Central Java Province of; Wonosobo, Banjarnegara, Batang, Pekalongan, Kendal and Temanggung (Figure 3.1). The location lies on the height of 1600 – 2100 meters above sea level and surrounded by volcanic peaks rising to 2200-2565 meter (Miller et al. 1983). In general, there is no definite border of Dieng volcano. The border of study area is the natural cliff of an old volcano that surrounds the Dieng plateau.

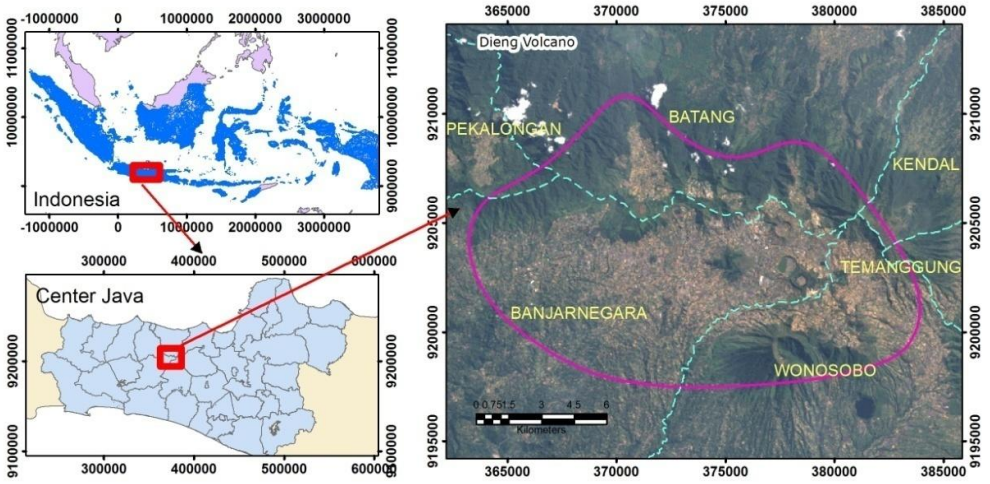

Source: Landsat ETM+ from http://glovis.usgs.gov/ and administration map from Geospatial Information Board (BIG) of Indonesia

Figure 3.1. Map of the study area. The area within the purple line is the study area, the light blue is the district border. All the maps in this research use coordinate system UTM zone 49S.

Dieng volcano has 9 craters which are dispersed at the East and West part of the area, namely: Sikidang, Sileri, Sibanteng, Timbang, Sinila, Condrodimuko, Siglagah, Bitingan and Pagarkandang. Two craters of Sikidang and Sileri have large craters and easy to access. In normal activity, both craters release the highest concentration of gases. The other craters are located in narrow and undulating

slope and produce lower concentration of gases.

The gases measurement is mainly concentrated in two craters of Sikidang and Sileri, considering its gases concentration and width of the area. While, the structural geology measurement is more focused on the depression area indicates a fault or joint.

Dieng has a hydrothermal system which is characterized by fumaroles, solfataras, mud pool and hot spring (Figure 3.2). Phereatic eruptions on Dieng occurred several times which are shown by the appearances of the abundant craters in the eastern part and central part as well as in the western part (Allard et al. 1989).

Figure 3.2. The indication of hydrothermal activity in Dieng volcano. (a. Gases release from Sikidang crater, b. Fracture that releases gases in Timbang, c. Mud pool in Sileri and d. Sulfatara in Sikidang crater)

Toxic gases and phreatic eruption usually affect a local area. Its impact is less if no human activity in the surronding craters. However, Dieng volcano is a plateau with fertile volcanic soil. It's average temperature between $12^{o}C$ – $20^{o}C$ on the day and $6^{o}C$ – $10^{o}C$ on the night, which make Dieng suitable for the vegetables crops. This condition encourages people to settle in Dieng plateau. Human activities have been increased significantly since 1975. Those marked by large scale of land clearing for potato crop (Arbangiyah 2012). Potato is a cash

crop that gives a high income for the smallholders in Dieng plateau. It can grow well in any type of slopes; therefore the smallholders not just cultivate the potato on the flate area but also on the slopy area. The prone areas to toxic gas hazards are also occupied by cultivation activities (Figure 3.3).

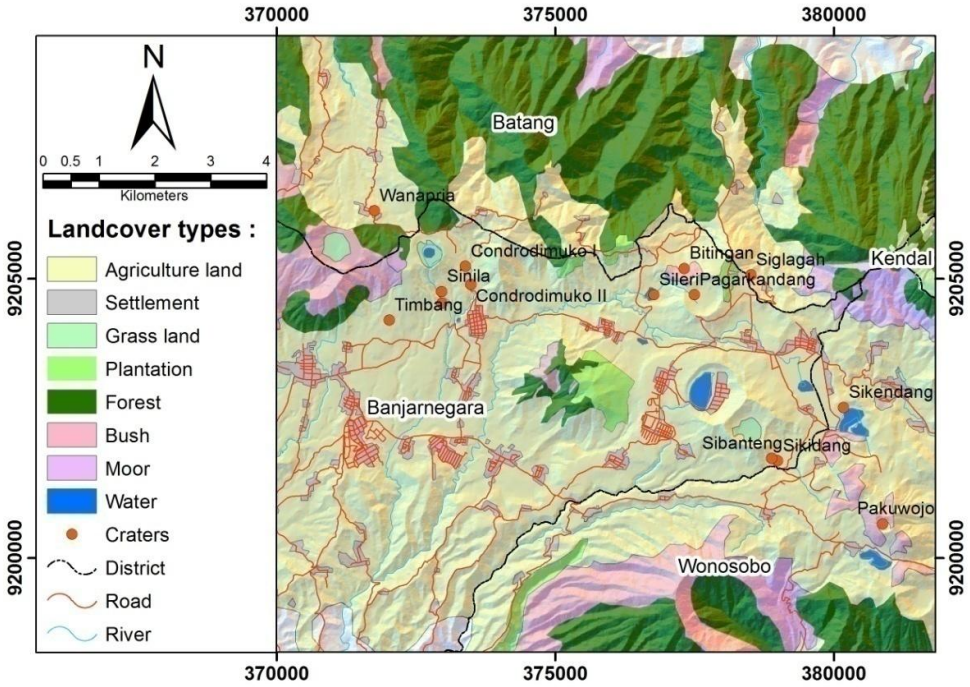

Source: Landcover map from Sabo office of General Work Ministry of Indonesia.
Figure 3.3. The 2010 landcover map of Dieng.

Moreover, the beautiful scenery, the rich of the history, and the development of the road infrastructure attract the people to come to Dieng, which make Dieng plateau as one of the tourist destinations. The uniqueness of the craters has become one of the tourist attractions. One of major issue is the development of waterpark nearby the Sileri crater (Figure 3.4).

The number of hazardouse craters, the increasing of local activity and the tourism activity increase the risk of toxic gases hazard and phreatic eruption in Dieng volcano. Therefore, the enhancement of the knowledge and the surveillance of the volcano become an important issue.

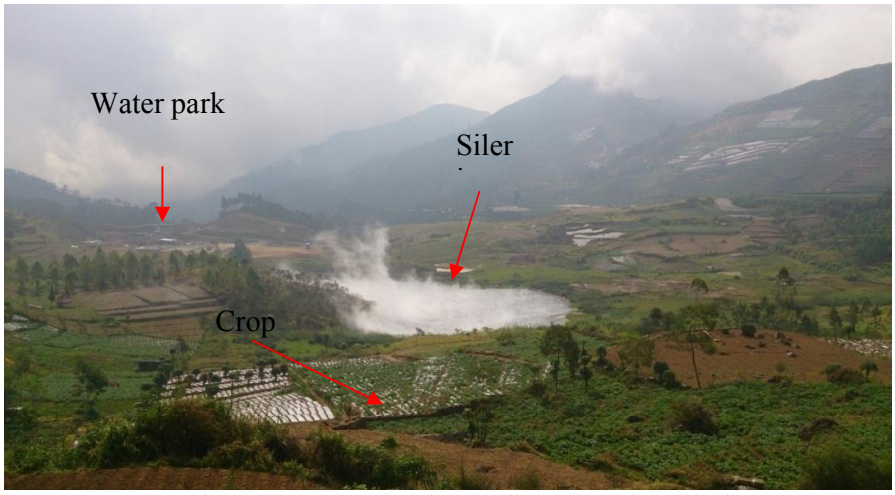

Figure 3.4. Waterpark constructions and crop fields nearby Sileri crater.

3.2. Summary of Dieng Volcano Activity

Dieng volcano has been documented since 1825. Its volcanic activities are dominated by phreatic eruptions and toxic gases outbursts events. The largest phreatic eruptions were recorded in 1944 in Sileri crater and in 1979 in Sinila crater. The phreatic eruption in Sinila crater coincided with toxic gases outbursts event in Timbang crater.

Phreatic eruption in 1944 in Sileri crater was reported to effect 38 people dead, 55 lost, 38 injured and a village disappeared. While, the phreatic eruption and toxic gases outburst event on February 20th, 1979 killed 142 people from Kepucukan village (Guern et al. 1982). Gases measurement on July 14th, 1979 showed that the toxic gas composition was mainly CO_2 (98,2%) with small amount of SO_2, CO, H_2S, HCN, HF, Cl and Cl_2.

In the period of 2008-2014, prior to the existing of Dieng seismic data, the phreatic eruption occurred once in Sileri crater on 27th September 2009. A report from Volcano Monitoring officer, the eruption did not give any sign of seismic activity increasing while toxic gases outburst events occurred two times in Timbang crater. The first period was on 28th May – 1th June 2011 where the gases reached the distance of 350 meters from the crater. The second was on 11th – 15th March 2013 where the gases reached the distance of 2000 meters from the crater.

Chapter 4. Research Methodology

Used method in this research is provided in this chapter including the required data, softwares, tools and analysis.

4.1. Required Data

The data required in this research are the toxic gases data, seismic data, ASTER images data, digital elevation model (DEM) data and seismo-volcano feature data.

4.1.1. Toxic gases data

Planned gases data were from the MultiGAS reader of Sileri and Timbang crater, which consisted of CO_2, SO_2 and H_2S gases. The MultiGAS reader is equipped with an automatic calibration and filtered from the active carbon to reduce the error in data acquistion. The data are taken per 1 minute. They are stored in the temporary storage in the tool prior to be sent to main computer in the office thru radio transmission per 6 hours. Unfortunatelly, the PVMBG is still developing the MultiGAS detector tools and they restrict to utilize the data for this research. Thus, the main problem during the fieldwork was to collect a complete data of CO_2 and SO_2 from PVMBG.

Another available data is from Investigation and Technological Development of Geological Disaster Board (BPPTKG). The data acquisition also used the same method with MultiGAS reader. However, it just has one sensor to acquire CO_2 data. The data is only available in Timbang crater. Daily measurement had been taken from 2011 until 2012.

Moreover, field measurement of SO_2 emissions using Drager X-am 5000 was conducted during ASTER data acquisition, especially in the area of the craters and fractures zones. The aim of the field measurement is to compare spatial patterns measured on the ground at exactly the overflight time to the retrieved SO_2 gas emissions patterns from the satellite data.

4.1.2. The Seismic Data

The seismicity data in the study area are consisted of the daily VT event (VTA, and VTB) and local tectonic earthquake. The tremor, gas burst and low-frequency are not included since they occur in the same time with the toxic gases outburst events. The seismicity measurement uses PS-21 recorder and seismometer L4C. The sensor is located in four locations; Timbang crater (07^{o} 11' 54,42" S and 109^{o} 50' 26,53" E on the high of 1783 m above sea level), Sileri crater (07^{o}11'24.02'' S and 109^{o}53'02.02'' E on the high of 1972 m asl), Mt. Pangonan (07 ^{o}12'51.88'' S and 109 ^{o} 53' 42.81" E on the high of 2296 asl) and Mt. Prau (07 ^{o} 11' 44.24" S and 109 ^{o}55' 04.58" E on the high of 2323 asl) .

4.1.3. TIR images data

ASTER images that were considered for this research are listed in Table 4.1 and Table 4.2. ASTER daytime has a nadir viewing image and a backward viewing image (Urai 2004). They were taken at different time, where backward viewing images were taken after the nadir images. This condition allows the calculation of wind velocity and wind direction that could be used in SO_2 flux retrieval. ASTER nighttime reduces the solar heating effect when used for temperature extraction (van der Meer et al. 2014).

There are two categories of ASTER data in this research. ASTER inside the fieldwork time and ASTER outside the fieldwork time. In the case of ASTER inside the fieldwork time, there were three date of ASTER scenes, acquired in9th October 2014, 25th October 2014 and 10th November 2014 (Table 4.1). However, just scene from 25th October 2014 was a meaningful one for the analysis, because the other two were either out of the study area or covered by a dense cloud.

Table 4.1. Scheduled ASTER acquisitions over study area during fieldwork.

No	Date	Day/Night	Time	Note
1.	9th October 2014	Day	03:05 utc or 10:05 local time	Out of Study area
2.	25th October 2014	Day	03:05 utc or 10:05 local time	Partly cloud
3.	10th November 2014	Day	03:05 utc or 10:05 local time	Dense cloud

ASTER scenes from outside of fieldwork window are also used for the purpose of thermal and SO_2 flux analysis. There are seven free cloud scenes; three from night-time ASTER scenes and four for day-time ASTER scenes (Table 4.2).

Table 4.2. Scheduled ASTER acquisitions over study area outside fieldwork window.

No	Date	Day/Night	Time
1.	9th October 2003	Day	03:05 utc or 10:05 local time
2.	2nd October 2005	Night	15:17 utc or 22:17 local time
3.	3rd October 2006	Day	03:05 utc or 10:05 local time
4.	4th July 2007	Night	15:17 utc or 22:17 local time
5.	6th July 2007	Night	15:17 utc or 22:17 local time
6.	14th April 2012	Day	03:05 utc or 10:05 local time
7.	29th June 2012	Day	03:05 utc or 10:05 local time

4.1.4. Digital elevation model (DEM)

The DEM sources data are the digital contour map, and Shuttle Radar Topographic Mission (SRTM) data. The contour map is from the Geospatial Information Board (BIG) of Indonesia. It has a 12.5 meter height interval range. SRTM data is from CGIAR Consortium for Spatial Information (http://srtm.csi.cgiar.org). It has a spatial resolution of 90 meter and a vertical error less than 16 meter. The DEM was processed to obtain 3D view of study area. It was used for fault analysis, temperature correction, and improving the visualization of resulted maps.

4.1.5. Landsat ETM+

The landsat ETM+ data was obtained from USGS earthexplorer (http://earthexplorer.usgs.gov/). It has spatial resolution of 30 meter for the visible, near infrared and sort-wave infrared. The Lansat ETM+ was used for the extraction of lineament.

4.2. Materials

The softwares to be used in this research are showed in Table 4.3.

Table 4.3. The softwares for processing data

No	Softwares	Functions
1.	R	Statistical analysis
2.	Envi 5.1	Digital images processing
3.	MODTRANT	Modeling Radiative Transfer Function
4.	PCI Geomatica 2015	Automatic lineament extraction
5.	Rockwork 16	Trend analysis of lineament
4.	ArcGIS 10.2	Visualization map
5.	Microsoft office 2010	Writing Report

The fieldwork tools to be used in this research are showed in Table 4.4.

Table 4.4. The tools for fieldwork activities

No	Tools	Functions
1.	Trigger X-am 5000	Measuring volcanic gases
2.	GPS Navigation	Plotting locations
3.	Digital pocket camera	Taking pictures in the field
4.	Topographical Map (RBI)	Guidance in the field

4.3. Research methods

Research method is divided into three sub-methods, field work, time series statistical analysis, and images processing.

4.3.1 Fieldwork

The field work consists of four activities which are (1) mobile gases measurement, (2) geological structure (GS) measurement,(3) inventory of gases emissions location, and (4) collecting daily seismic and gases data from Dieng volcano observatory office (Figure 4.1).

The mobile gases measurements were done during satellite over pass the area, dated from 2ndOctober 2014 to 10th November 2014 (Table 4.1). The result of measurement is stored in Appendix 1. The data from field measurement is compared with the gases data retrieved from imageries.

a. The first measurement was carried out on the 2nd of October 2014. It was done by measuring the gases on the surrounding of Sikidang, Sileri, Condrodimuko and Sibanteng craters.
b. The measurements in 9th, and 25th of October 2014 used a transect method which took two directions; the purpose is to know the distribution of gases concentration in each location at that time.
c. In 10th of November 2014 the cloud was very dense, therefore the measurement was not conducted, considering that the ASTER image at that time would be covered by the cloud.

Figure 4.1. The fieldwork activities (a. Measuring gases, b. Entry data, c.Measuring geological structures)

The measurement of geological structure (GS) is aimed to construct the fault system in the Dieng. The measurement found 15 locations of of GS. The locations of 15 points GS measurement can be seen in Figure 4.2.a. The GS are categorized in to three types in the study area. First, joints were found almost in all of 15 measurement location. Second, fault planes were found in Timbang, River, Merdada and Sileri. Last, fault scarps were found in Pagakandang. The detail results of GS measurements are shown in Appendix 2.

The inventory of gases emission location was done during fieldwork activities. It was found that the gases are emitted from 14 locations in Dieng. 9 locations emit gases and hot spring and the other emit only gases, detail can be seen in Table 4.5. Figure 4.2.b shows the distribution of gases emission in Dieng volcano. The distribution forms clusters which are concentrated in East part and West part of the Dieng volcano.

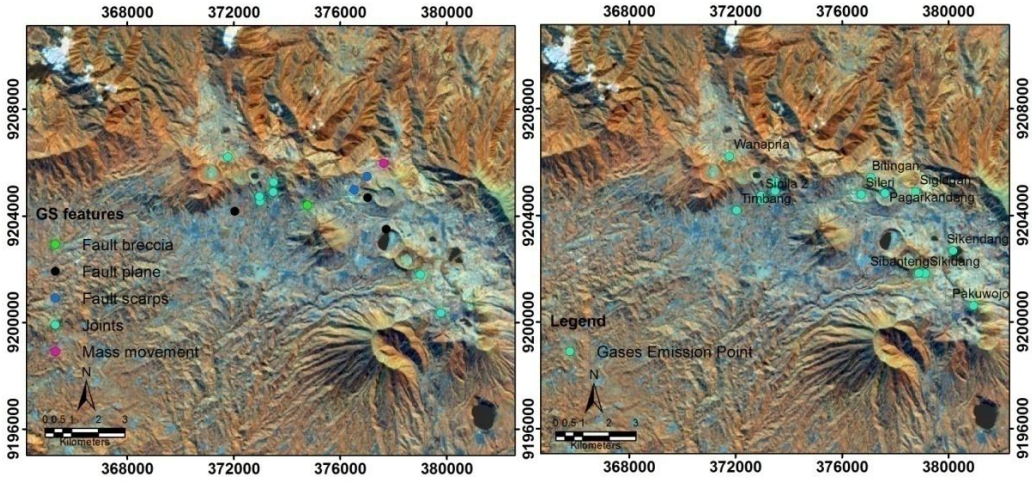

Figure 4.2. Map locations of fieldworks. (a. the geological structure measurement, b. gases emission inventory)

Table 4.5. The craters and fractures where the gases emited.

NO	X	Y	Location	Decription
1	109.8408	-7.19693	Timbang	Gases
2	109.899	-7.19023	Siglagah	Gases
3	109.8535	-7.18913	Condrodimuko I	Gases and hot spring
4	109.8839	-7.19347	Sileri	Gases and hot spring
5	109.904	-7.22042	Sikidang	Gases
6	109.903	-7.22005	Sibanteng	Gases and hot spring
7	109.914	-7.213	Sikendang	Gases and hot spring
8	109.8909	-7.19357	Pagarkandang	Gases and hot spring
9	109.8542	-7.19171	Condrodimuko II	Gases and hot spring
10	109.921	-7.23068	Pakuwojo	Gases and hot spring
11	109.8871	-7.18809	Bitingan	Gases
12	109.8494	-7.19284	Sinila 1	Gases and hot spring
13	109.8496	-7.19491	Sinila 2	Gases in patato field
14	109.8387	-7.17982	Wanapria	Gases and hot spring

Seismic data was collected by using PS-21 recorder and seismometer L4C. The data that was stored in Volcanic Observatory office of Dieng from 9th of August 2008 to 13th of November 2014. The data consist of deep volcanic (VA), shallow volcanic (VB), local tectonic (TL) and far tectonic (TJ) data.

There was only one seismograph recorded the data from 9th of August 2008 to 10th of April 2013. The additional three equipments were installed in

different locations on 11th April 2013. Using four seismographs, the epicenter of volcanic and tectonic earthquakes were detected. The analysis of epicenter from April 2013 to December 2013 for a big scale earthquakes were conducted by the volcanic observatory office of Dieng volcano. The results are shown in Figure 4.3. These data is very useful to analyze the triggering factor of gases emission in April 2013.

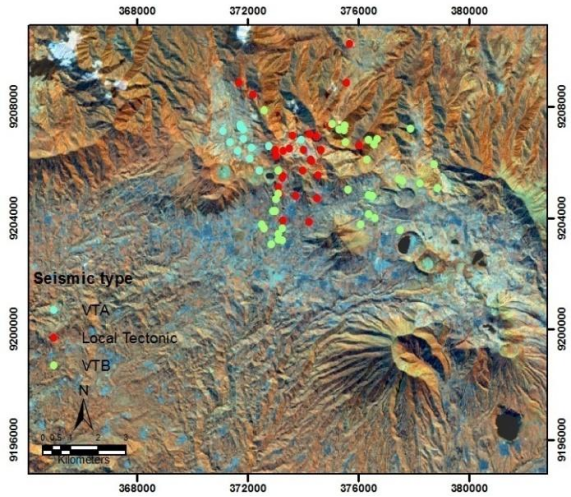

Figure 4.3. The epicenters of different earthquakes. (VTA-light blue, VTB-light green and local tectonic-red)

4.3.2 Fault analysis

The steps to follow in the fault analysis are summarized in the Figure 4.4 which is carried out in three stages:

a) Images preparation
b) Fault lineament extraction
c) Faut verification

Image preparation

Raw data of contour map and Landsat ETM+ need to be preprocessed to meet the requirement of the analysis. Contour map uses to build the digital elevation model (DEM) with 12.5 meter vertical interval which high enough to be used for a further analysis. The interpolation procedure has been done to produce DEM image. The used method is the Australian National University DEM

(ANUDEM). The ANUDEM is a surface fitting approach which produces DEM from irregular spaced elevation (Gallant & Hutchinson 1997). The advantages of applying the ANUDEM is that it can generate a better interpolaton of ridges and stream areas (Arun 2013). The DEM image further is used to build hill-shade image. The hill-shade image is produced in three stages which are integrated in DEM Visualization tool in ILWIS. The first stage is created three direction of shadow images (West, Nort West, and North) using shadow filters. The second stage uses the linear stretching to stretch the three shadow images which produce 24-bit color composite image. The last stage is removing the temporary three shadow images and representing the color composite shadow images.

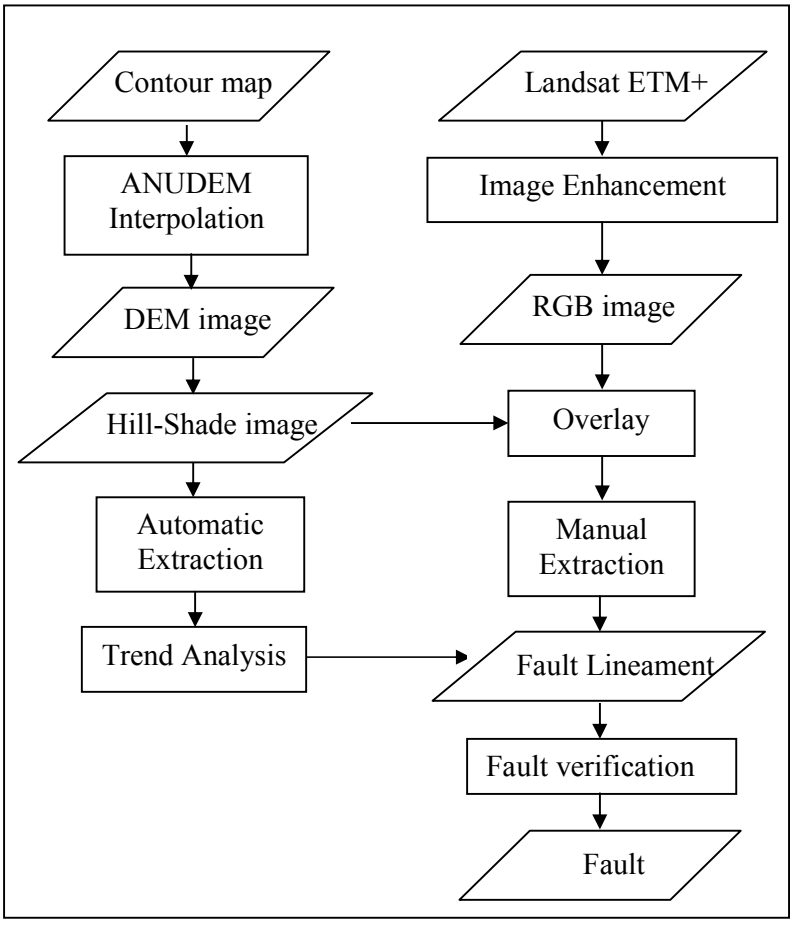

Figure 4.4. The flow diagram of fault analysis.

The original Landsat ETM+ data in the first display have a dark appearance cuased by low brightness and contrast level of the image. A linear contrast enhancement or contrast stretching is used to enhance the appearance of the image which applies a minimum-maximum contrast stretch method. The minimum-maximum contrast stretch method stretches the minimum and maximum value (original) of the image to a newly specified set of values which optimizes the full lenght of brightness values of the image (Al-amri et al. 2010).

Lineament Extraction

Based on the fact that the geological features can be geometrically identified as a linear or curvy line (lineament) on the surface of the earth (Bonetto et al. 2015). The geological features can be extracted from the topographic or remote sensing images as a lineament. The lineament extraction follows two steps; manual extraction and automatic extraction. Manual extraction used the visual interpretation of the operator to extrapolate the linear features. It is hightly efficient at extracting lineament. The manual extraction aims to extract the main lineament. The used of the overlayed hill-shaded DEM and Landsat ETM+ images would enhance the visual appearance of linear features, which would help in the extrapolating.

Automatic extraction uses numeric method for lineament detection and extraction. The hill-shaded DEM data was used to extract the lineament using edge-detection algorithm which is a code built in *PCI Geomatica* (Sukamar et al. 2014).The algorithm follows two steps (Hashim et al. 2013). Firstly, edge detection operator produces a binary image. It utilizes Gaussian filter which is known to be an effective in detection and localization. Secondly, line detection extracts continuous line segments. It uses a pixel connectivity-edge linking algorithm which connects all corresponding line edge pixels. The automatic lineament detection was extracted the lineament from a small to large size. Further, the results were used for trend analysis. The trend analysis was done to know the dominan direction of the lineament as well as to analyze the direction of the main force structural geology. It based on the start and end coordinates of the

lineament, which transform to the bearing data using the *Rockwork 16* line analysis. The bearing data then constructs the rose diagram which represents the direction trend of lineament. The lineament trend and main force were used to construct the geological structure mechanism in study area. Thus, the combination of the lineament from manual extraction and main force could give the information about the fault type and process.

Fault verification

Fault lineament can be mixed with geomorphological features and artificial features (Hashim et al. 2013). The most common method to prove the fault lineament is by measuring and analyzing the fault products such as; joint, fault planes and fault breccias in the area that has already been identified as a fault zone. The field data further could be used for verifying the fault.

Correlation between fault zone, craters and earthquake epicenter

The correlation between fault zone, earthquake epicenter, and craters was done by overlying the fault with the earthquake epicenter and location of craters.The active fault is marked by the earthquake activity. The overlying of fault and local earthquake could inform the status of the fault. The overlying of fault and crater location could provide the information about the role of the different types of fault to the distributions and types of craters in Dieng volcano.

4.3.3 Time Series Statistical Analysis

Time series statistical analysis is divided into 2 steps cyclical pattern analysis of time series and cross correlation analysis of time series.

Cyclical Pattern Analysis of Time Series

The statistic time series analysis uses the spectral analysis method which works based on the Fast Fourier Transform (FFT) process for local tectonic, VTA and VTB time series data. The spectral density has advantages when examining the periodic characteristics of a time-series offers an efficient means (Nicholson et

al. 2013). It calculates the time series data in the frequency domain, which is directly related to the autocovariance of time series.

Which coefficient

$$f(\omega) = \gamma_o[1 + 2\sum_{i}^{\infty} \rho_t cos(\omega_t)] \quad (3)$$

ω_t is the frequency expressed as cycles per unit of time

γ_o is the overall covariance sequence

The spectral density estimation uses periodogram, which relates the density to the frequency (Rossiter 2012). The periodogram measures the relative importance of possible frequency values that might explain the oscillation pattern of the observed data. It is a squared correlation between the time series X and the sine/cosine waves. The coefficient is:

$$I(\omega) = \frac{1}{n}\left|\sum_{t} e^{-i\omega t} Xt\right|^2 \quad (4)$$

However, the raw periodogram is too rough in estimating the population of spectral density. The smoothing procedur using Daniell kernel and tapering methods can define spectral density over a continuum of frequencies. The Daniell kernel with parameter *m* works based on centered moving average. It creates a smoothed value at time *t* by averaging all values between times *t* – *m* and *t* + *m*. While, tapering method would weight the ends of the series less than the center of the data.

Cross Correlation Time Series

This phase aims to correlate the pattern of local tectonic earthquake with the pattern of VT and CO_2. This uses procedure of the bounded together two or more time-series. The procedure is provided in R using cross *ts. Intersect* and *ts.union* functions (Rossiter 2012). Furthermore, the correlation value between two or more time-series data can be obtained from the cross-correlation function (CCF) by specifying the first variable as a leading factor for the second variable. Formula to be used in this step is based on (Matthews et al. 2009).

Correlation coefficient:

$$\varphi = \frac{\sum[x(i) - mean(x)]x\,[y(i - lag) - mean(y)]}{\sqrt{\sum[x(i) - mean(x)]^2}\,x\sqrt{\sum(y(i - lag) - mean(y)]^2}} \quad (5)$$

Where, X is time series x

Y is time series y

The maximum correlation is not always occurring in the lag 0 (same time). The positive lag means that the first variable leads the second variable. While negative lag means the second variable tends to lead the first variable. There is also a positive cross-correlation value which indicates the relative above value of the first variable leads to the relative above value of the second variable and negative correlation value mean that the relative above value of first variable leads to the relative below value of second variable.

The application of cross-correlation to a single shock event represents the process of tranfering and modifying energy from the input to the output during the major events (Mayaud et al. 2014) such toxic gases outburst events. It also shows an impulse respone which occurs in the system.

4.3.4 SO_2 Retrieval

The remote sensing-based SO_2 retrieval is divided into three steps, SO_2 gas plume detection, SO_2 retrieval scheme, and SO_2 emission map evaluation. Five cloud free ASTER day time scenes were used to retrieve the SO_2 fluxs in Dieng volcano. ASTER daytime scene is advantageous because it has the availability of nadir and backward looking images which can provide wind velocity data (Urai 2004). The scenes acquired on 9th October 2003, 3rd October 2006, 14th April 2012, 29th June 2012 and 25th October 2014. Unfortunately, the scenes on the eruption time were not successfully obtained, because at that time ASTER did not acquire data or there was covered by dense cloud.

Gas plume detection

An existence of gas plume in the image is important for SO_2 retrieval. The gas flume detection is done using band rationing of ASTER (B10+B12)/(2*B11). The band ratios of (B12+B10)/(2*B11) is used to improve the presence of the plumes (Campion et al. 2010). An SO_2 plume is characterized by an accumulation of pixels with the ratio >1 in the form of cluster or contiguous. The categorized area, further is selected as the calculation area for SO_2 flux retrieval. Two areas of special interest are Sikidang and Sileri craters. Both craters emit high concentration of SO_2.

SO_2 Retrieval Scheme

The retrieval of SO_2 uses the Radiative Transfer Simulations method by fitting the ASTER band ratios (B10+B12)/(2*B11) and B14/B11 (Campion et al. 2010). This combination had been proven to reduce the effects of surface emissivity, plume temperature, surface altitude and atmospheric humidity. SO_2 is highly absorbing at wavelength between 8.1 and 9.5 μm, most strongly affecting ASTER band 11. The general equation for measuring the radiance L_s value of SO_2 column amount from TIR radiative transfer is given below. For the clarity, the wavelength dependency is omitted. The first term is an emitted Planck radiance from the Earth surface at temperature T_0. The second term is a reflected downwelling radiance which can be excluded in the absence of sun glint. The third term is an emitted upwelling from each layer of the atmosphere including the plume.

$$Ls = \varepsilon . B(T) . t_0 + (1 - \varepsilon) L_d . t_0 + \int_0^A B(T_z) . \frac{\partial t_z}{\partial z} dz \qquad (6)$$

Where,
B(T) : blackbody Planck function for temperature T,

Ɛ : the surface emissivity

z : altitude

0 : altitude of the surface

A : altitude of the sensor

t_z : transmittance between altitude z and A

L_d : downwelling radiance

The simulation of SO_2 column amount employs MODTRAN radiative transfer code (Urai 2004).

In order to produce 3D matrixes consisted of the radiance values of each SO_2 column amount, the plume altitude and ground temperature for each band (5 TIR bands) is produced. Beside that, the simulated spectra is also integrated on the spectral response function of ASTER. The variety of surface temperatures and surface types under the plume is retrieved from a SO_2-free region as described in the LST extraction stage. The Visible-Near-Infrared (VNIR) images are used to get the wind speed and plume altitude. ASTER provides nadir and backward looking images in each scene. Where, the backward looking image is taken after nadir. This different time acquisition provides the displacement of plume images information that can be used to calculate the wind speed and plume altitude (Urai 2004).

When the information about radiance ratio, surface temperature and plume altitude are obtained, the SO_2 column amount can be interpolated into the 3D matrix of the simulated spectral radiance ratio. The fitted ASTER band ratio (B10+B12)/(2B11) is firstly used to retrieve the SO_2 column amount, only for the results below 15 g/m^2. If that is higher, the band ratio (B14/B11) is used to avoid saturation effects. Lastly, the SO_2 emissions are modeled from the SO_2 column amount by multiplying its traverse with the wind speed.

Evaluation of retrieved SO_2 map

Evaluation of the retrieved SO_2 map is based on the field measurement of SO_2 emissions in the same date with the ASTER acquisiton. The image of 25th October 2014 has the same date with the field measurement of SO_2 emissions. The field data is acquired at the time close the time ASTER overpass Dieng area in two craters Sikidang and Sileri by using portable device. The amount of SO_2 emissions released from each crater is also calculated. Those are used as a reference for the plumes amount in the

atmosphere. Other images are compered with the average SO_2 emissions from the automated measurement of SO_2 emissions. This evaluation is performed to know how well the retrieved SO_2 flux data in Dieng volcano.

4.3.5 Thermal Anomaly Detection

The thermal anomaly detection is followed three steps: thermal atmospheric correction, LST extraction, and surface kinetic temperature correction.

Thermal Atmospheric Correction

Satellite-based TIR images rely on the surface parameter (temperature and emissivity) and the atmospheric effect (Li et al. 2013). The atmospheric effect can affect the accuracy of the deriveted LST therefore the raw TIR image needs to be corrected to get better retrieval results.

The atmospheric correction uses the In-Scene Atmospheric Compensation algorithm (ISAC) (DiStasio & Resmini 2010) including the thermal atmospheric correction tool of ENVI. ISAC assumes that a near-blackbody surface appears within the scene and the atmosphere is similar along the data scene. The algorithm will first determine the wavelength that most frequently indicates the maximum brightness temperature. The wavelength would then be used as the reference. The formula to be used is:

$$L_s = tB(T) + L_u \quad (7)$$

Where, L_s = at-aparture radiance
t = transmission of the atmosphere
$B(T)$ = Planck function
L_u = upwelling radiance due to the atmosphere

LST Extraction

The LST extraction uses the Temperature emissivity separation (TES) method. TES is amethod that extracts the temperature and emissivity at once

(Coll et al. 2007). It has advantages to generate unbiase and pricise emissivity in the first generation of calculation which could improve the LST result. It would extract 1 temperature and 5 emissivity images.

The calculation of temperature and emissivity consists of the following modules (after Gillespie et al. (1998)):

1. Normalized Emissivity Method (NEM) module: NEM calculates the maximum temperature using the at-ground radiances Eq.(2) with an estimated L_d and estimated Ɛ (0.97). The initial emissivity is obtained from the maximum temperature.
2. Ratio module: It uses for the estimation of the first T and $Ɛ_j$ by calculating β-spectrum. β-spectrum is a value of relative emissivity which is calculated from the radiance emitted by the surface ($L_{e,j}$), j is the five band of ASTER TIR image, using formula

$$\beta_j = \frac{L_{e,j}}{B_j(T)} \frac{B}{L_e} \quad (8)$$

The $L_{e,j}$ can be obtained from the formula

$$L_{e,j} = L_{g,j} - (1 - \varepsilon_j) L_{d,j}/\pi \quad (9)$$

Where, L_e = the average of $L_{e,j}$ for the five ASTER TIR band

B = the average $B_j(T)$ for the five ASTER TIR band.

3. Min-Max Difference (MMD) module: the βj needs to be scaled to get the actual emissivity value. The steps to be followed are:
   Calculation of MMD using the following formula:

$$MMD = \max(\beta_j) - \min(\beta_j) \quad (10)$$

The minimum emissivity is (ε_{min}) calculated according to the laboratory spectral measurement of different landcovers. The formula to be used is

$$\varepsilon_{min} = 0.993 - 0.687\ x\ MMD^{0.73\ 7} \quad (11)$$

The actual emissivity is calculated using the formula

$$\varepsilon_j = \beta_j \varepsilon_{min} / \min(\beta_j) \quad (12)$$

Finally, the actual LST is calculated using Eq. (2) with the new emissivity estimation. All the procedures are integrated in one software of ENVI. The user just defines the estimated value of emissivity.

Surface Kinetic Temperature Correction

Surface kinetic temperatures were corrected for lapse rate (drop in temperature with altitude) and illumination effects (warmer slopes towards the daytime sun exposure) using the so-colled "STcorr" code built by Ulusoy et al. (2012) in Interactive Data Language (IDL). The STcorr is specially designed for correcting ASTER nighttime images. However, it can be used to other nighttime images. The STcorr based on a simple regression method which corrects the surface kinetic temperature (ST) image using three steps: lapse rate/altitude, aspect and slope correction. It is a continue process, where the result of altitude corrected temperature is used for aspect correction and the corrected aspect temperature is utilized for slope correction. The slope-corrected temperature is the end result of topographic correction (Figure 4.5). The ST images are the LST images acquired from ASTER TIR images. The DEM image is taken from the SRTM. Aspect and slope images are modeled from the DEM.

Thermal anomaly is determined from a simple statistic calculation. The mean and standard deviation values are obtained from the area within Dieng volcano by applying masking procedure to exlude outside area from the calculation. High anomaly areas are also exluded to get average temperature value and to avoid high standard deviation. The value above threshold (mean + n*standard deviation) is considered as the anomaly of the temperature. Where, n value is range from 1, 2 and 3 which correspond with 92%, 95% and 98% confidence level respectively.

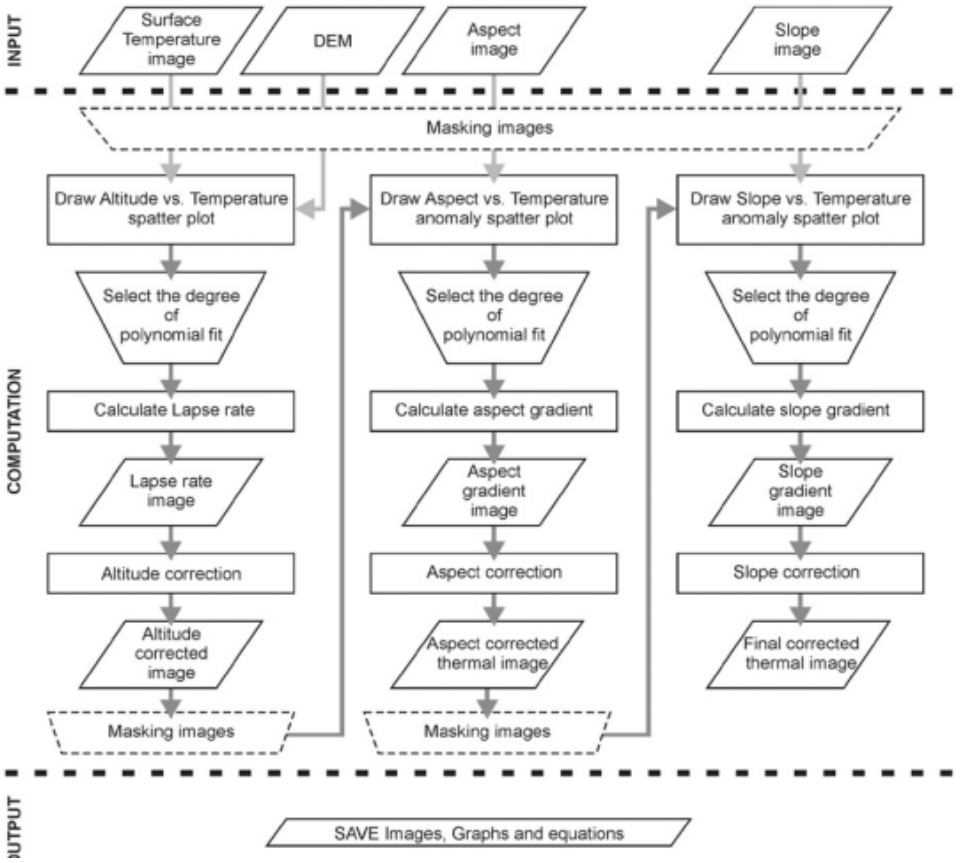

Figure 4.5. The continues process of STcorr (after Ulusoy et al. (2012))

Chapter 5. Results and Discussion

This chapter provides information regarding the characteristic and distribution of the craters, time series analysis, SO_2 retrieval and surface temperature anomaly.

5.1 Characteristic and Distribution of the Craters

Dieng volcano activity spreads within several craters distributed along the eroded caldera of Dieng plateau. The craters of Dieng volcano are famous for their toxic gases outbursts and phreatic eruptions (Allard et al. 1989). The examination of the craters' characteristic and distribution are based on two steps: the craters characterization and fault lineament analysis.

5.1.1 Characteristic of the Craters

Based on the field work measurement, the gases in Dieng volcano consists of three main constituents namely SO_2, H_2S and CO_2. These constituents have various concentrations in each crater in Dieng volcano. Two most prominent craters that release toxic gases are Sikidang and Sileri (Appendix 1). Normaly, Sikidang crater emits SO_2, H_2S and CO_2 between 2 – 126.1 ppm, 0.6 - 66 ppm, and 0 – 2 % mol. respectively. Meanwhile, Sileri crater releases SO_2 from 0.6 - 10 ppm, H_2S from 0.5- 5 ppm H_2S, and CO_2 0 - 0.3 % mol.. The gas distributions in the craters rely on the distance from the fracture and wind direction. However, in case of CO_2, topographic condition will affect the distribution and the flow of the gas (Guern et al. 1982). In Dieng, there are two major areas which differ based on the volcanic manifestations: the Eastern part of Dieng area and the Western part of Dieng area. In this research, the Eastern part of Dieng area is represented by Sikidang and Sileri craters, and the Western part of Dieng area is represented by Timbang and Condrodimuko craters.

Sikidang is the largest crater in Dieng. It has 82.164,2 m^2 areas, in total (Figure 5.1). The gases are released from several fractures in the crater area. It has

two main fractures, Sikidang and Sibanteng. The gases is mostly distirubuted in Sikidang fracture with varies concentration from 9 – 126.1 ppm. The highest SO_2 concentration is on the South West (SW) part of the fracture which is affected by the wind blow. Sikidang fracture crates the plume with diameter $\pm$ 10 – 30 meters and height $\pm$ 100 – 150 meters. Sibanteng fracture releases smaller amounth of SO_2. The concentrations are varies from 5 – 11 ppm and disapper when they reach 10 meters height. On the North (N) and North East (NE) part of the crater the SO_2 concentration is relatively low between 0 – 5 ppm. The gases are usually emitted from small fractures on the area.

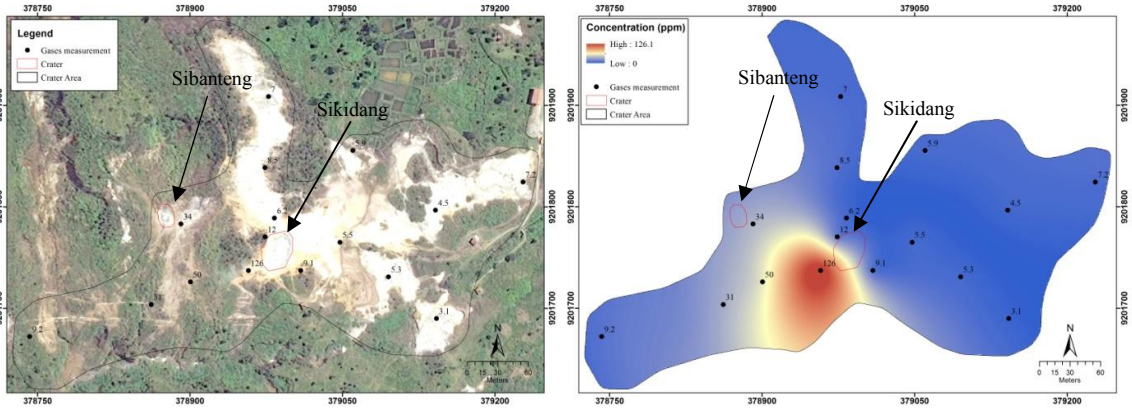

Figure 5.1. Map of Sikidang crater. The left side is Quickbird image of Sikidang, which is bordered by black line. Bare area affected by heat and gases emission from fractures in the area. The right side is a gas distribution which is interpolated from point measurement of 9th October 2014 using ANUDEM method. The distribution shows that the highest concentration of gases is on the fracture area to the southern part because the wind flows to the South at the time of measurement.

Sileri is the second largest crater in Dieng with total area up to 65.947,4 m^2. Different with Sikidang crater, Sileri crater has a lake with 11.039,8 m^2 width (Figure 5.2). The lake has metalic color and froth affected by the hydrothermal system underneath the crater. The gases are released from the lake and several fractures in the area. The SO_2 gas from lake is concentrated on the E part of the area due to wind blow. Its concentrations are varies from 0.4 -10.1 ppm. Moderat

SO_2 concentrated on the N part is from the fracture in the area. During the fieldwork, the crater does not form a plume. The gases are dispersed when they reach the height of 20 meter. One Multi-gas reader has been installed in this area. However, the data is restricted to be used for comparation with the mobile measurement data.

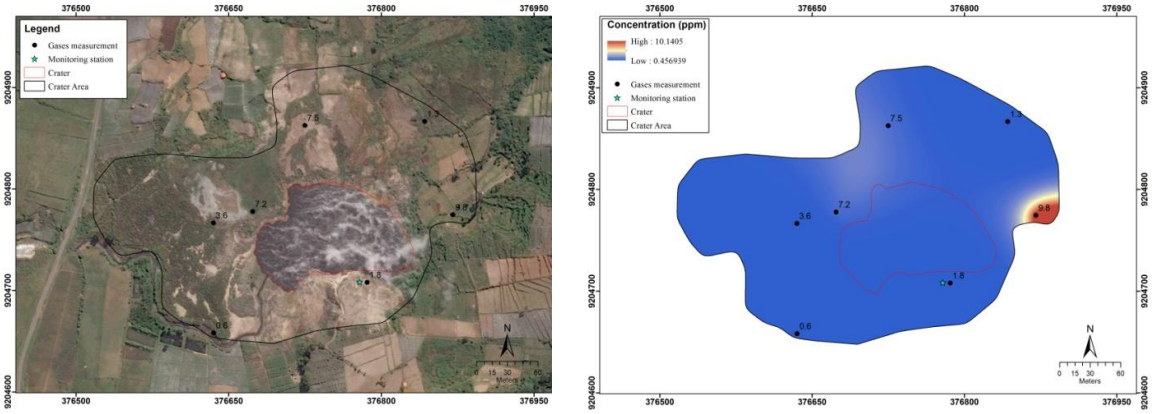

Figure 5.2. Map of Sileri crater. The left side is Quickbird image of Sileri, area in the red polygon is Lake of Sileri. The right side is gas distributions interpolated from point measurement in 9th of October 20014 using ANUDEM method. The distribution shows that the highest concentration of gases is on the NorthEast part of the lake because the wind flows to the area in measurement times.

Figure 5.1 and Figure 5.2 have shown different between Sikidang and Sileri craters. The gases in Sikidang crater are emitted to SW part of crater controlled by the several fractures in the area, while the gases in Sileri crater are released to E part of the Crater Lake. The Crater Lake controls the emitting gases in Sileri crater. The different in gases direction is affected by micro-topography different between them (Kondo et al. 2002). The North East part of Sikidang is a large plat area while in the South West part is a hilly area. As well, Sileri has a flat area in the West part and hilly area in the East part. It shows that wind tends to blow from plat or lower area to hilly area. The amount of SO_2 concentration is also different between Sikidang and Sileri crater. Sikidang crater releases SO_2 gas 12 times larger than Sileri crater. This difference can be affected by the characteristic of craters. Sikidang is a fumarolic field while Sileri is a Crater Lake.

Fumarolic field is reported to has higher temperature and can produce higher concentration of gases than Crater lake (Kalacheva et al. 2015).

In the West part, the craters are characterized by narrow craters and single fracture for gases releasement. Timbang crater is unreachable during the fieldwork due to difficult access and unsafe condition (daily CO_2 emission). It can be seen in Figure 5.3.a. that the gases are emitted from single fracture which is located between the cliffs. Whereas, Condrodimuko is more accessible and safe (Figure 5.3.b). It has a fracture which releases 2 – 9.9 ppm SO_2, 1 – 6.1 ppm H_2S and 0 – 0.3 % mol. CO_2 (Appendix 1). It is also located within narrow cliffs as Timbang crater. Condrodimuko crater also discharges hot spring which make the gases concentration almost similar with Sileri crater.

From above explanation, the East part (Sikidang and Sileri) and the West part (Timbang and Sikidang) craters are different in the area settings and the gases releasement. The East part craters are located in quite large area and gentle slope. They also have several fractures for the gases emissions. Meanwhile, West part have small craters which are located in an undulating to steep slope. The gases usually release from single fracture. These phenomena will be discussed by analyzing the fault lineament analysis in the next sub-chapter (sub-chapter 5.1.2).

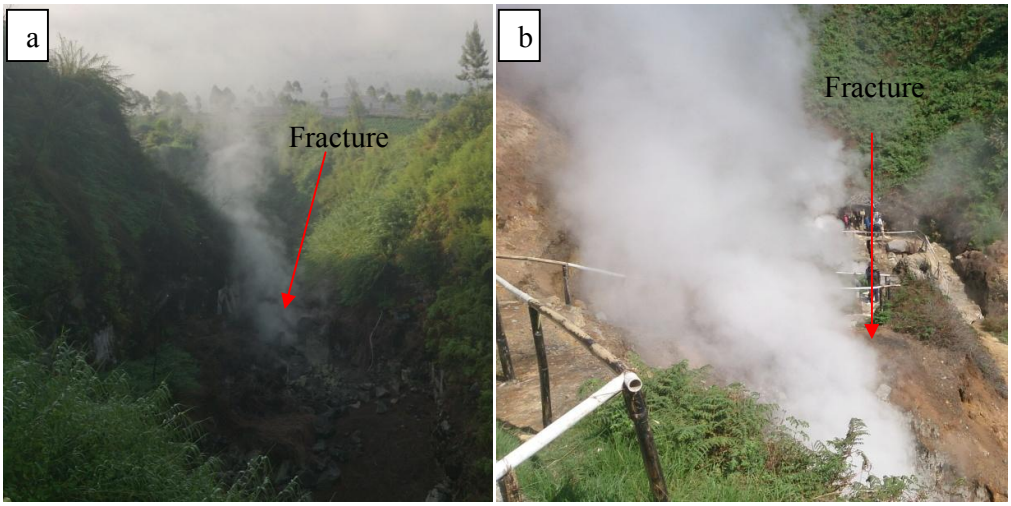

Figure 5.3. The gases release from single fracture of Timbang (a) and Condrodimuko (b).

5.1.2 Fault Lineament Analysis

Figure 5.4.a shows the result of manual lineament extraction. The extraction uses Landsat ETM+ map which was overlaid by hillshade with 70% transparence to visualize the topographical setting of the area. The morphologic model indicates four important lineaments. Three lineaments (L1, L2 and L4) have NW - SE direction and one lineament has NE - SW direction. The relief models of the lineaments are shown by Figure 5.4.b. First lineament (L1) is represented by large depression in Northen part of L1 and cutting hill in the middle area near to Timbang crater. The second lineament (L2) is indicated by straight ridge of hills from NW to SE of L2. The third lineament (L3) is represented by dominant straight morphology in the East part of the study area. The fourth lineament (L4) is shown by straight ridge in the NW part of lineament and fault scraps near to Sileri crater. It correlates with the depression which forms inactive lakes of Dieng, Telaga Warna and Pengilon in the middle to the South East part of L4.

An automatic lineaments extraction result is shown by Figure 5.4.c. It extracts the lineament based on the same hill-shaded relief model of DEM map with manual lineaments extraction technique. The extracted lineaments are diverse in the size from few meters to hundreds meters. Most of the lineaments represent the manifestation of geological structure which is also clarified the result of manual extraction by comparing both of them. The four lineaments from manual extraction appear as concatenated lines patterns in the extracted lineaments. The morphologic effects such cone of the hills, gully and edge of the old caldera are still visible in the map. This is due to the contrast edge lines which is formed by that morphologic features in the input image (Hashim et al. 2013). However, considering the small number of them, they can be neglected.

Furthermore, the extracted lineaments are used to analyze the dominant azimuth using trend analysis. The trend analysis used the starting and the ending coordinates of individual line of automated lineaments. It represents dominant

directions of lineaments: North-South and North West – South East (Figure 5.4.d). The azimuth of the main tectonic stress of lineaments (δ_1) is obtained from the average of two most frequencies direction of lineaments resulting value of 350^o. The δ_1 direction can be used to analize the type of faults in the area by comparing its value with the four lineaments direction. The four main lineaments are categorized as strike-slip faults. The angles between the faults and the δ_1 are less than 45^oC (Jordan et al. 2005).

The Figure 5.4.c also shows the correlation between extracted lineaments and field data. The field data of geological structure can prove lineaments as faults. Comprehensive data of field measurement of geological structure is attached in Appendix 2. There are four main geological structure data in the study area which are fault planes, fault breccias, fault scraps and joints. The dominant directions of joints are from 330^o - 40^o. The fault planes and fault breccias directions in several locations are between 350^o - 10^o.

Two field measurements of fault plane and joints are located close to L1. The fault plane consists of fault plane, fault breccias and net slip. Their directions are 159^o, 167^o and 175^o respectively. Joints have two main directions 10^o and 40^o. This indicates that L1 is in accordance with the field data. One fault breccia and four joints points are located close to L2. The fault breccia has direction of 350^o and the joints have main directions 350^o and 30^o. This direction also shows a similarity with the L2 direction. The four joints are also situated close to L3. L3 has different direction with L2, however same tectonic stress can generate couple strike-slip faults with the relative angles less than 45^o to the tectonic stress direction (Jordan et al. 2005). Two fault planes, two fault scarps and joints are located near to L4. Their directions are 225^o-245^o, 185^o-315^o and 20^o-60^o respectively. The fault scraps directions are almost similar with L4 direction, however fault planes have different directions with L4 direction. The fault planes locations are not exactly in the zone passed by L4, therefore they may be generated by small faults activities not by L4.

In general, geological structure measurements data meet the agreements with manual and automatic lineaments which are shown by the azimuth similarity between them. This proves that the four main lineaments are faults. The faults are also in accordance with two lineaments resulted from residual magnetic anomalies which have same direction (NW – SE) with L2 and L4 (Geological Agency of Indonesia n.d.).

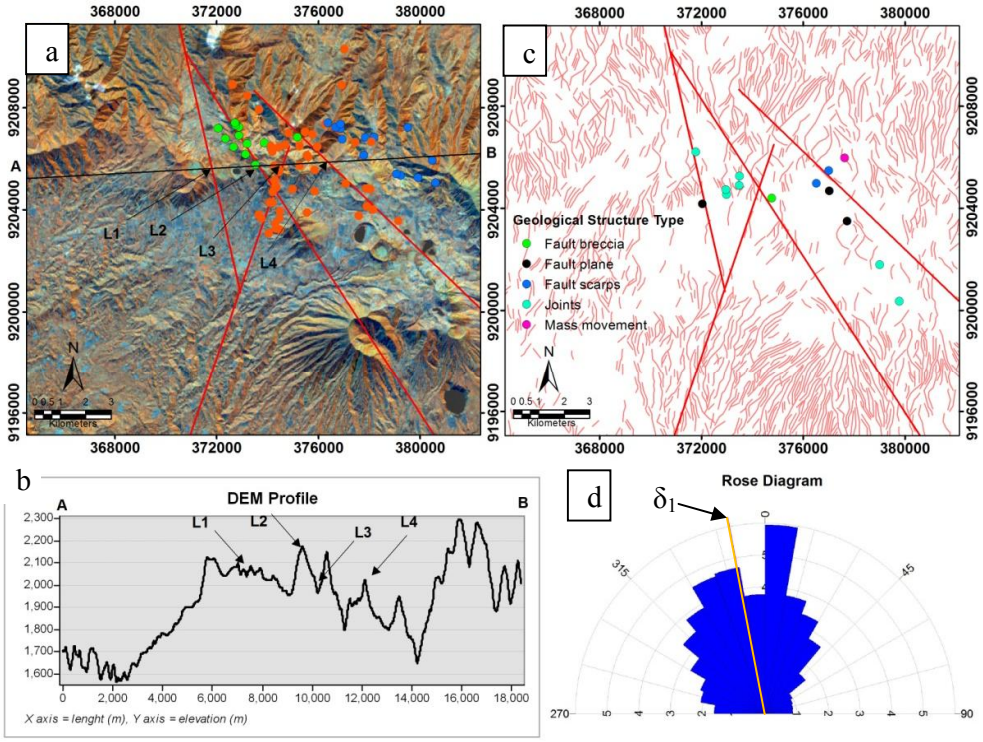

Figure 5.4. Map of fault analysis. a. Manual lineament interpretation from Landsat ETM+ and hill-shade maps. The red lines show the lineament and the black line is a cross line for DEM profile ; b. DEM profile of cross line A-B which shows the relief of lineament L1, L2, L3 and L4; c. The comparation map of automatic lineaments extraction (pink line), manual lineaments extraction (red line) and field data (points); d. Fan diagram shows the trend direction of lineaments and main tectonic stress direction (orange line).

The faults were compared with the earthquake epicenters data to know the correlation between earthquakes activities and their generated faults. Their comparisons were represented in Figure 5.5.a. The earthquakes activities are

concentrated in the middle part of study area near to the West part craters. They are dominated by local tectonic earthquakes. Their events have formed two straight patterns which correlate to L3 and L4 faults. This indicates that the force L3 and L4 generate their events. This also indicates that L3 and L4 as active faults system because the local tectonic earthquake has a correlation with an active fault (Zielke et al. 2015). VTA earthquake is concentrated in the Northern part of L2 fault. It usually correlates with force of magma to uplift which forms cracks in the wall rocks that generate earthquakes (Zlotnicki et al. 2000). Since L2 fault is coupled with L3 fault, local tectonic earthquakes events can also affect the area in L2 fault zone which can trigger the VTA events along the L2 fault zone. VTB earthquakes do not correlate with tectonic activities. Their events are distributed in the North East part of study area out of the zones of 4 identified faults.

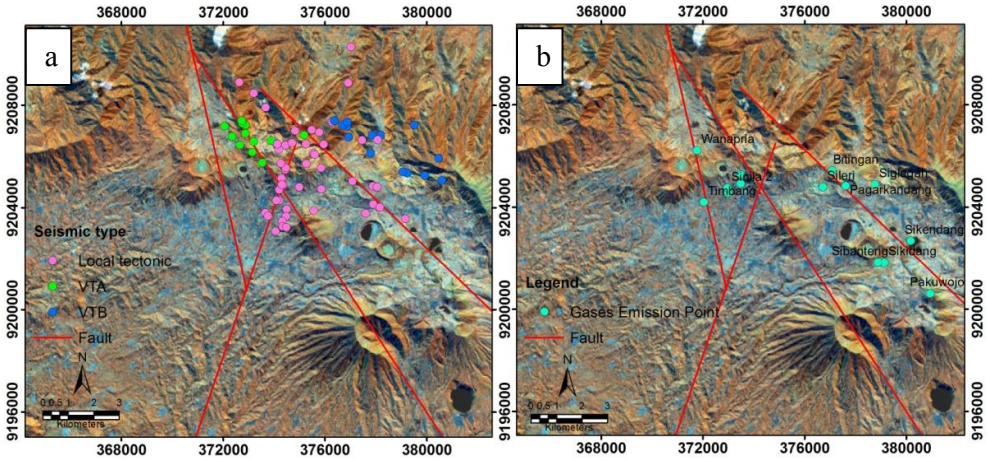

Figure 5.5. The correlation map between a. fault and seismic epicenter and b. fault and emission points.

The faults data are then compared with the gases emission points inventory data. Thier comparison are shown in Figure 5.5.b. There are 14 gases emission points in the study area which associate with fumaroles (Sikidang, Sibanteng, Timbang, Sikendang, Bitingan, Pagarkandang and Siglagah), hot springs (Sileri, Wanapria, and Condrodimuko), and mud volcano (Sikidang, Sibanteng and Sileri). The gases emissions points are categorized into two main faults system which are West zone and East zone. The West zone is passed by several faults (L1, L2 and L3) which forms complexs fault system. The gases

emissions points (craters) which associate with this system are Timbang, Condrodimuko, Wanapria and Sinila. They are characterized by small and narrow craters which dominantly produces CO_2 when they erupt. While the East zone is only passed by L4 fault. The craters which associate with this zone are Sileri, Sikidang, Sibanteng, Siglagah, Bitingan, Sikendang, Pakuwojo, and Pagarkandang. They are characterized by large crater. In the historical events, phreatic eruption and mud volcano occured in several craters of this system. Time series analysis of seismic and CO_2 data explain further regarding this phenomenon.

5.2 Cyclical Period of Tectonic and Volcano Tectonic Earthquake

In most volcanoes, the local tectonic earthquakes events are not correlated with the VT features while, the VT earthquakes (VTA and VTB) occur as a series of events during volcanic unrest activity (Jousset et al. 2013). However, in Dieng volcano, the local tectonic earthquakes and VT earthquakes can be series of events because the systems that control the volcano are hydrothermal system and tectonic system. The cyclical pattern analysis can reveal the periodical pattern of local tectonic and VT earthquakes in relations with the toxic gases outburst events and phreatic eruption.

The analysis of cyclical period uses spectral density analysis working due to fourier transform (Nicholson et al. 2013). Three datasets of local tectonic, VTA and VTB were analyzed. The result of analysis is shown by the graph of the spectrum value and frequency domain in Figure 5.6. The strongest spectrum value shows a time different between two highest peak of frequency which is considered as the cyclical pattern of time series (Rossiter 2012).

The local tectonic represents two peaks of spectrum (Figure 5.6.a). The strongest spectrum is within frequency of 0.006510417 associated with the cycle of 153.6 days. The weaker spectrum is in frequency of 0.0334201389 or 29.9 days. The first peak correlates to the cyclical period of the local tectonic earthquake and the second peak is an anomaly caused by an artifact of the

particular data series (Rossiter 2012). The VTA shows one strongest spectrum at frequency of 0.003472222 related to 288 days cycle period (Figure 5.6.b). The VTB shows strongest spectrum value at frequency of 0.002170139 which correlates with the 460.8 days cycle period (Figure 5.6.c).

The results show that cyclical periods of the local tectonics, VTA, and VTB are different. The cyclical period of the local tectonic earthquake event is almost equal to two times of the VTA and three times of the VTB. This indicates that local tectonic earthquake as an independent variable has no direct correlation to the VT process (Budi-santoso et al. 2013). The periodical event of the local tectonic earthquake tends to be controlled by the fault system, instead of VT process. Meanwhile, the different cyclical periods between VTA and VTB events show that the deep volcanic process is not always continue to shallow volcanic process. Therefore, VTA earthquakes are not always followed by VTB earthquakes as series events.

None of the cyclical periods of seismic types have correlation with the periods of toxic gases outburst event. The two recorded Timbang toxic gases outburst events (on March 2011 and May 2013) have time lags of 650 days which means Timbang has 4 times of local tectonic earthquakes and 2 times of VTA earthquakes. The VTB earthquakes have the closest cyclical period with time lags, which is 190 days time difference. The VTB earthquakes period also does not show a correlation, considering the duration of toxic gases outburst events are less than 1 month. This indicates that the seismic earthquakes are not always followed by the toxic gases outburst events. The relation between seismic events and toxic gases outburst will then be explained by cross correlation analysis in the next sub-chapter (sub-chapter 5.2.1).

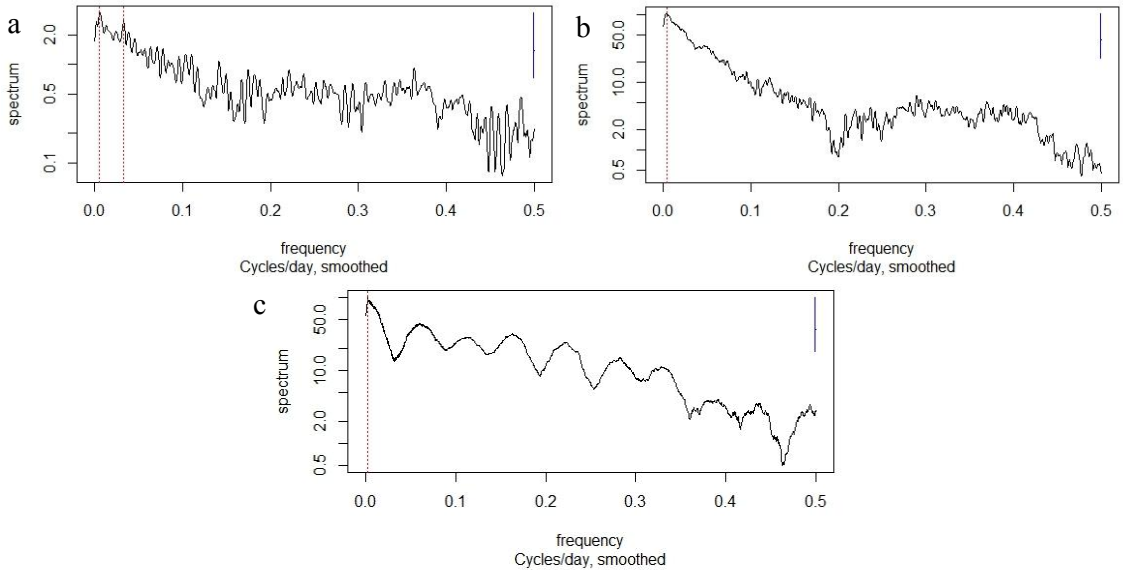

Figure 5.6. The graph of spectral density from three seismic features. (a. Spectral density of local tectonic, b. Spectral density of VTA and c. Spectral density of VTB.The red vertical dash shows the strongest spectrum, the blue vertical dash represents the 95% confidence level). Multi-Parameters Cross Correlation

5.2.1 The Cross Correlation of Seismic Data

Seismic data from 9thAugust 2008 to 13th November 2014 has been established to analyze the correlation between local tectonic earthquake and VT events. Two main volcanic events are detected from the increasing of seismic frequencies. There is a correlation between the local tectonic earthquake events and the increasing of VT events. The correlation results can be shown by the red dash correlation of the three graphs (local tectonic earthquake, VTA and VTB) (Figure 5.7.a.b.c). Figure 5.7.a.b.c shows that local tectonic earthquake, VTA and VTB has occurred simultaneously during volcanic unrest activity in Dieng volcano.

There is one interesting finding that needs to be concerned; a phreatic eruption recorded in Sileri crater on 27th September 2009 has no correlation with any event either seismic events or toxic gases outburst events. This indicates that

the phreatic eruption is mainly caused by the hydrothermal process in the area and it does not depend on tectonic and VT process. The phreatic eruption does not cause the occurrence of toxic gases outburst events. Based on this finding, the monitoring of phreatic eruption using another approach needs to be adressed since the seismic events cannot explain the phreatic eruption causation.

Moreover, the toxic gases outburst event represents high correlation with strong magnitude of local tectonic earthquakes. The local tectonic earthquakes with magnitude above 3.5 in the richter scale or above $1.5x10^{17}$ in the earthquake energy corresponds with the increasing events of the VTA and VTB and the events of two toxic gases outburst which can be seen in Figure 5.7.d.e. This indicates that local tectonic earthquake has an important role to the volcanic toxic gases outburst events, and also to the increasing of volcano-tecstonic signals.

The correlation is also represented by CCF analysis. The time series of local tectonic earthquake has been compared with the VTA and VTB as shown in graphs in the Figure 5.8.d.e.f and its values in the Table 5.1. The graph correlation between local tectonic and VTA earthquake shows that the auto correlation fungtion has the highest value on the zero lag (64,3%) and the dominant correlations are on the positive lags. It is indicated that most of local tectonic and VTA earthquakes occurs in the same days which local tectonic earthquakes tend to lead the events. The cross correlation between local tectonic and VTB earthquakes also shown a same pattern with low correlation values. The maximum correlation is (35,5%) which indicates the local tectonic earthquakes has lesser possibility to be followed by VTB earthquakes compares to the VTA earthquakes events. The VTA also has been correlated with VTB and the highest cross correlation value is 69,2 %. The comparation also represents the same pattern with two previous graphs where the highest correlation occurs in 0 lag and most of correlations are on the positive lags. The VTA and VTB have high correlation value which is denoted that VTA events would be potentially followed by VTB events.

The cross correlation results of seismic features are in line with the result of faults and epicenter correlation. The epicenter of local tectonic earthquakes in the West zone faults have correlation with VTA earthquakes, while VTB earthquakes are not correlated with fault zones. The correlation results are also consistent with the previous cyclical pattern analysis. The closer cyclical period between local tectonic earthquake and VTA is represented by the higher correlation between them, likewise between VTA and VTB. Meanwhile, lower correlation between local tectonic earthquake and VTB is shown by the low correlation between them.

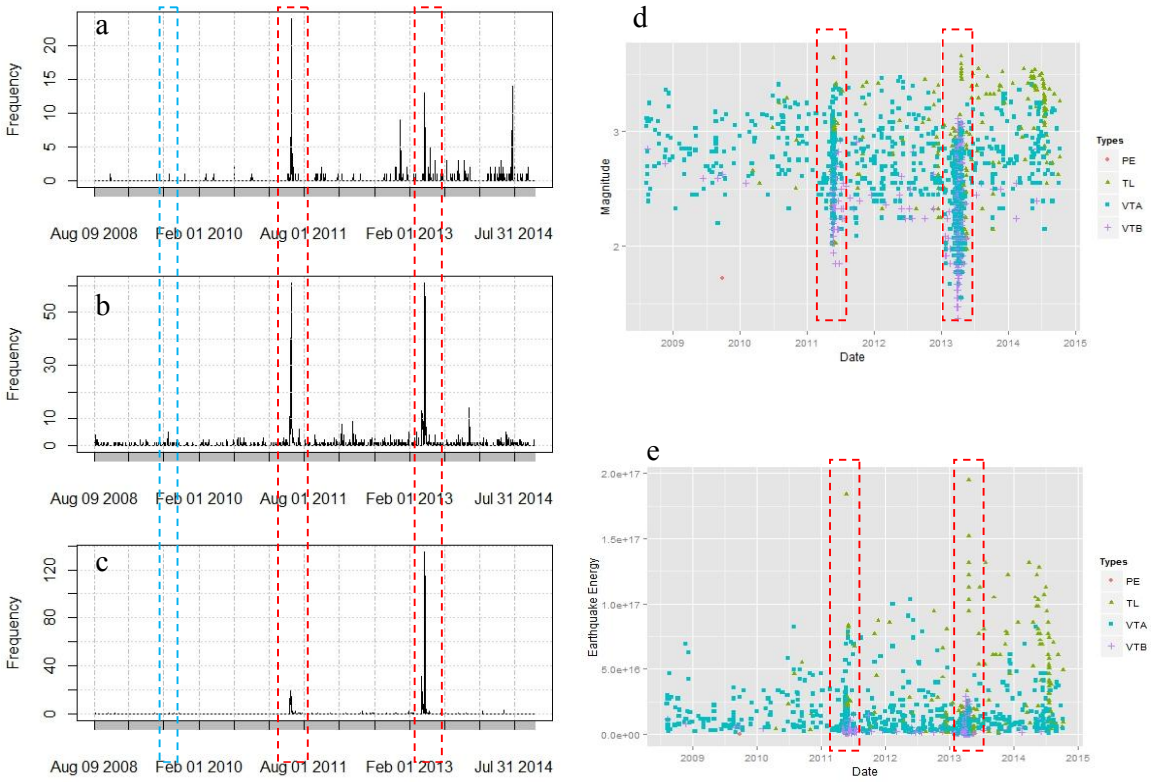

Figure 5.7. Frequency, magnitude and energy of time series seismic events. (a. frequency of local tectonic earthquake, b. frequency of VTA earthquake, c. frequency of VTB earthquake, d. Earthquakes magnitude, e. Earthquakes energy, PE: phreactic eruption, Red dash shows the events of toxic gases outbursts in March 2011 and May 2013 with high frequency and magnitude of seismic. Blue dash represents the event of phreatic eruption in September 2009 without sign of increasing seismic activity and toxic gases outburst event)

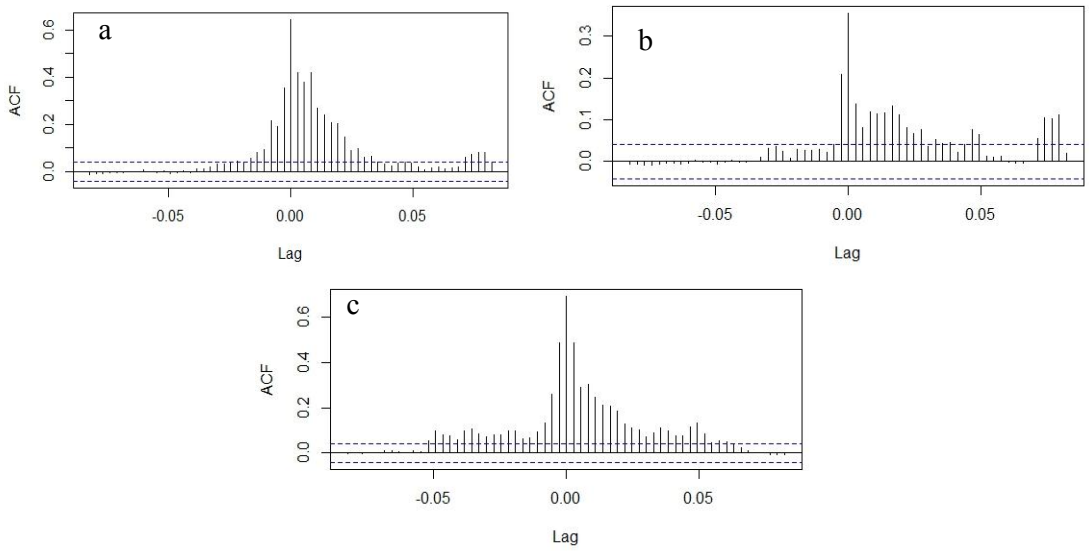

Figure 5.8. The CCF correlation results of tectonic earthquake and VT earthquake. (a. the CCF between the local tectonic earthquake and VTA, e. the CCF between local tectonic earthquake and VTB, and f. the CCF between VTA and VTB).

Time series analysis of seismic data has revealed an understanding about periodical behaviour and correlation of the local tectonic and VT earthquakes. The local tectonic earthquake has shown a strong correlation with the deep volcanic process and represents a weak correlation with the shallow volcanic process. The strong correlation of local tectonic and VTA earthquakes makes Dieng volcano unique compared with the other volcano such as Merapi (Budi-santoso et al. 2013), where the local tectonic events are not give a significant impact to VT events. Deep volcanic process and shallow volcanic process of Dieng volcano represent a common process of volcanic unrest events where deep volcanic process is potentially followed by shallow volcanic process (Jousset et al. 2012).

The seismic features and toxic gases outburst events have shown the correlation in the context of magnitude and frequency of earthquakes, not in the context of periodical events. The toxic gases outburst events tend to occur in the events of strong magnitude of local tectonic earthquakes and high frequency of seismic events. Based on the fact, that the CO_2 gas is produced in deep magma chamber which usually released to the surface (Giggenbach et al. 1991). The cap

rock can trap the gases in shallow level, near to the surface. Strong energy and high frequency of seismic eartquakes could act as the trigger factor on releasement of the trapped CO_2.

Whereas, the phreatic eruption in Sileri is not related either by strong magnitude or peak frequency of seismic earthquakes. It also does not correlate with the toxic gases outburst events. Its process can be explained by the hydrothermal process beneath the crater lake where compression of hydrothermal energy can generate pressure to the hot spring and mud volcano eruption (Kalacheva et al. 2015).

Table 5.1. The CCF values between local tectonic earthquake, VTA and VTB.

Lag	TL - VA (%)	TL - VTB (%)	VA - VTB (%)
-10	3.2	3.6	8.1
-9	3.8	2.5	7.9
-8	4.6	0.7	10
-7	4.1	2.9	9.8
-6	5.6	2.8	6.5
-5	8.2	2.7	6.5
-4	9.2	2.8	9.2
-3	21.6	2.2	13.3
-2	19.3	4.2	26
-1	35.4	20.8	48.7
0	64.3	35.5	69.2
1	41.9	13.7	48.8
2	37.7	8.1	28.9
3	42	12	30.5
4	26.8	11.4	24.9
5	24.1	11.7	21.2
6	20.9	13.4	20.9
7	20.3	11.3	18.5
8	14.5	8.2	12.8
9	9	6.7	10.9
10	9.7	7.6	10

5.2.2 The Cross Correlation between Carbon Dioxide and Seismic Data

Two sets of data; the Carbon Dioxide (CO_2) from Timbang crater (taken from 4th April 2011 to 9th May 2012) and seismic data (local tectonic earthquake, VTA and VTB) are used for the cross correlation analysis. The time series data show an impulse respone (one toxic gases outburst event) which one recorded toxic gas outburst event within the time series. Considering the impulse respone, this analysis uses only the data during the toxic gases outburst event to avoid the effect of long 0 values in the seismic time series data to the correlation results. CO_2 data are documented in three types of data: minimum, average and maximum concentration. This analysis uses the maximum concentration of CO_2 data. Considering that the increasing CO_2 concentration is correlated with the toxic gases outburst events (Guern et al. 1982). The CO_2 and seismic data have also been analyzed by graph and cross correlation function (CCF) analysis.

Figure 5.9.a shows the graph of local tectonic, VTA, VTB and maximum CO_2 concentration. The local tectonic and VTA earthquakes show same patterns. The increasing frequency of local tectonic and VTA earthquakes start 3-4 days before toxic gases outburst. The highest frequency has only one day lag the toxic gases outburst event. The frequency of local tectonic and VTA earthquakes show sharply decrease during the toxic gases outburst with some pluctuation in the remaining times. The VTA earthquake represents slight different pattern. The increasing frequency was recorded from 12 to 13 days before the toxic gases outburst. The highest frequency occurs 8 days before the toxic gases outburst events and decrease significantly during the toxic gases outburst event. Since the peak event of VTB earthquakes has the longest delay times before the toxic gases outburst event, it can be a good sign for early warning sytem of future toxic gases outburst events.

Cross correlation between local tectonic earthquake and CO_2 emissions rate is shown by Figure 5.9.b. and table Table 5.2. It represents an undulating pattern which two peaks of correlation occur in the positive and negative lag. The

undulating pattern shows the process transferring and modifying energy which occur before and after the peak event (Mayaud et al. 2014), in this case is the toxic gases outburst event. The positive lags have shown negative correlations. The negative correlations pattern in positive lags show different aspect of the correlation. The constant reduction in CO_2 concentration over time lags occurs in relation to the peak events of local tectonic earthquakes. The highest correlation in 7 days lags (-40.7%) were correlated with the normal concentration of CO_2 gas emissions. This can be an indication of the duration of toxic gases outburst events in correlation with local tectonic earthquakes events. While positive correlation in negative lags show the continues fluctuating events of local tectonic earthquake during the toxic gases outburst event.

The same pattern is also shown by the cross correlation between VTA earthquake and CO_2 emission which can be seen in Figure 5.9.c. and Table 5.2. The peak of negative correlation occurs in 5 days positive lag which also indicates the toxic gases reach normal concentration after 5 days of the highest frequency of VTA earthquakes as shown by the peak correlation (-52.2%) in the time lags. The moderate frequency of VTA earthquakes also occur during the toxic gases outburst events which is shown by the moderate positive value correlation (38.2%) in negative lag.

The correlation between VTB and CO_2 emission is also shown same pattern but it has different interpretation (Figure 5.9.d). The patterns between VTB and CO_2 graphs do not show a significant relation between VTB and CO_2 patterns. This is caused by the presence of the time lag between the peak VTA earthquakes event and the toxic gases outburst event where during the time lag the CO_2 concentration is still normal as shown in Figure 5.9.a. While positive correlation in negative lags also represents the same continues pluctuating events of VTA earthquake as local tectonic and VTA earthquakes during the toxic gases outburst event. More detail correlation values are shown by Table 5.2.

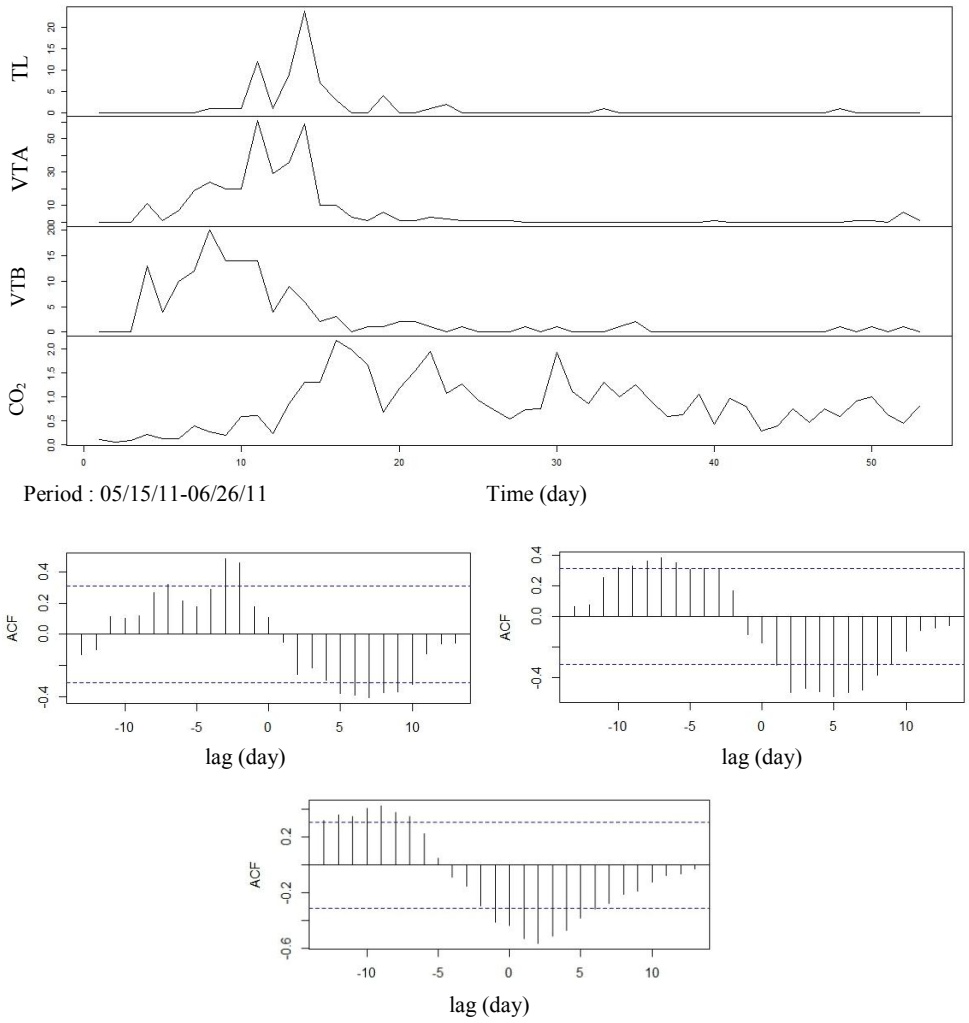

Figure 5.9. The graph correlation between local tectonic earthquake, VTA and VTB with CO_2 emission rate. (a. The graph of local tectonic earthquake (TL), VTA, VTB and CO_2 b. Cross correlation between local tectonic earthquake and CO_2, f. Cross correlation between VTA and CO_2, g. Cross correlation between VTB and CO_2)

The single shock event (one peak event) analysis of 2011 toxic gases outburst event using graph and CCF correlations reveals two different perspectives. The graph correlation show delay between seismic types events and the occurance of toxic gases outburst event. The peak events of local tectonic and VTA earthquakes have delay times 1-2 days and the peak events of VTB earthquakes have a longer delay times about 8 days. While, CCF correlation discribes the duration of toxic gases outburst event from the peak frequency of

seismic. However, a longer delay time between the peak frequency of VTB and the toxic gases outburt event make an error. In the case of correlation values, the fluctuation pattern of seismic events and CO_2 emission rates may affect to the medium values of the correlations (Nicholson et al. 2013).

Table 5.2. The CCF values between the seismic features and CO_2 emissions rate. (TL: local tectonic earthquake,CO_2: maximum CO_2 emission rate).

Lags	TL - CO_2 (%)	VTA - CO_2 (%)	VTB - CO_2 (%)
-10	9.9	31.7	40.8
-9	12.1	32.5	42.7
-8	26.8	35.9	38.1
-7	31.8	38.2	35
-6	21.6	34.9	22.6
-5	17.5	30.8	4.9
-4	28.6	31.1	-8.9
-3	48.5	31	-15.1
-2	45.7	16.7	-29.1
-1	17.4	-11.8	-41.2
0	10.9	-17.2	-43.8
1	-5.1	-31.7	-53
2	-25.9	-49.4	-56.4
3	-21.8	-47	-51.5
4	-29.8	-48.9	-47.2
5	-38	-52.2	-38
6	-39	-49.6	-31.9
7	-40.7	-47.7	-27.7
8	-37.6	-38.2	-20.8
9	-37.1	-30.6	-19
10	-32.1	-22.7	-12.3

5.3 SO_2 Retrieval

The result of the first step (band ratio) of the retrieval procedur is shown in Figure 5.10. The values of band ratios vary in each image between 0.97-1.04. The high values are mostly located on the hilly and mountaineous areas such as on the North part and upper part of Sikidang. This indicates that the high values are caused by topographic effects, not by plumes. None of the images has shown

patterns of cluster or continous which indicated the appearance of plumes on Sikidang and Sileri craters. The results clearly show that no plumes are detected from two areas target of Sikidang and Sileri craters in all five images.

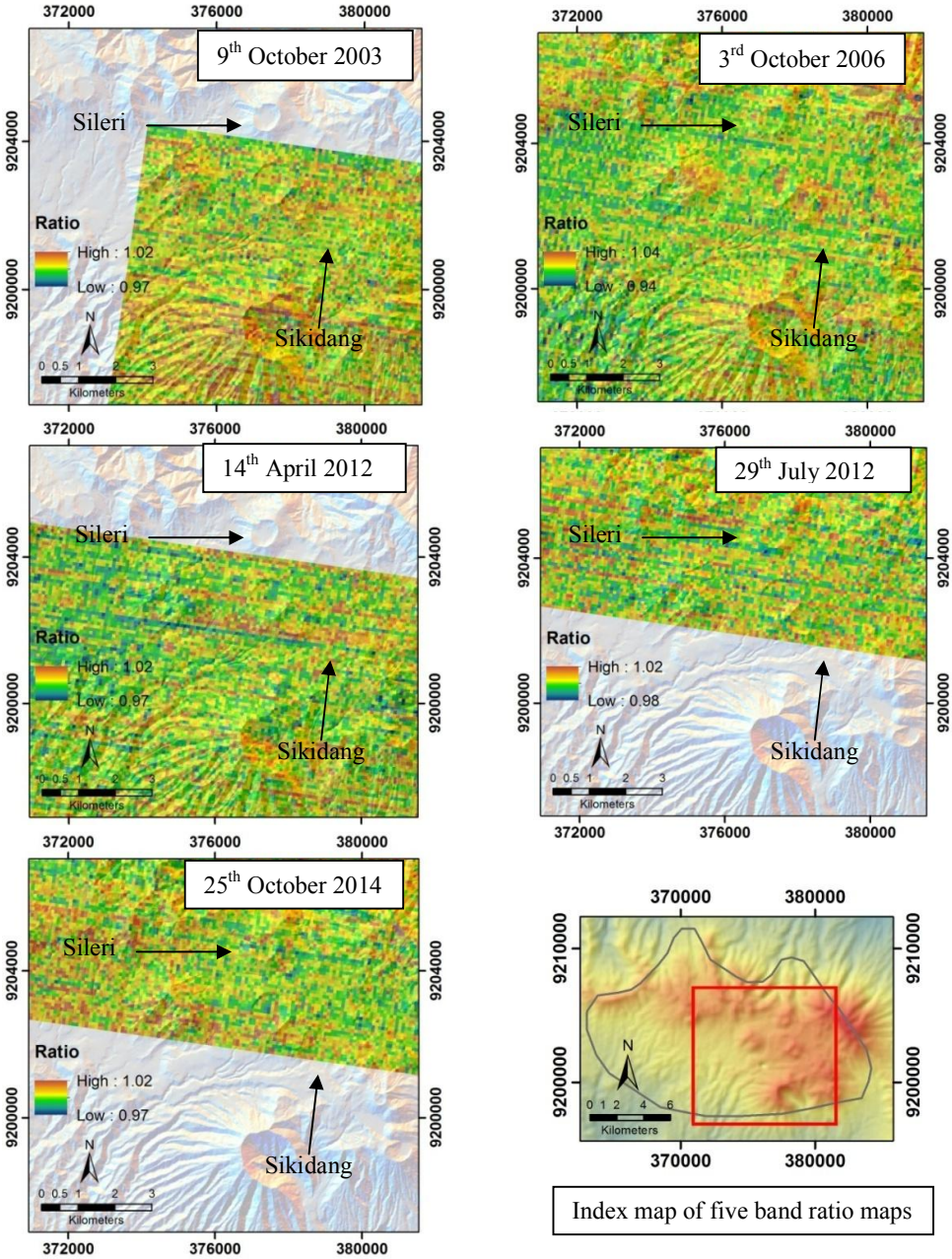

Figure 5.10. Band ratio of (B10+B12)/(2*B11 from six ASTER daytime TIR scenes which shows no pattern of SO_2 plumes on Sikidang and Sileri craters. The map was superimposed by DEM with 70% tranparancy.

It can be concluded that the number of plumes for normal condition within both craters (Sikidang and Sileri) as shown in Figure 5.1 and Figure 5.2 cannot be detected by the ASTER TIR image. The previous research suggests that the ASTER can detect SO_2 plumes within the scales of Miyakejima, Mt. Etna and Kilauea(Urai 2004; Pugnaghi et al. 2006). The absence of plume indicates that further analysis can not be continued.

5.4 SurfaceTemperature Anomaly

Dieng volcano is a quaternary volcanic complex which is categorized by geothermal features. Generally, geothermal features can be identified by the presence of thermal anomaly (Frondini et al. 2009). The craters of Dieng volcano have a various daily temperature between 58^{o}C – 92^{o}C (Table 5.3). Pagarkandang and Siglagah have the highest daily temperatures while, Sileri has the lowest daily temperatures. Based on the results that show that SO_2 did not affect the radiance of the ASTER TIR images in the Dieng area, the 5 bands of ASTER nighttime TIR images are used to analyze for potential thermal anomalies. The ASTER nighttime TIR images have advantages of a reduced solar heating influences (van der Meer et al. 2014), therefore more accurate temperature data can be obtained. Three cloud-free night time ASTER TIR images (2nd October 2005, 4th July 2007 and 6th July 2008) have been processed to get the thermal anomaly in the area.

Table 5.3. Daily normal temperatures in Dieng craters from 2013-2014.

Craters	Temperature (^{o}C)
Sileri	58 – 62
Sikidang	86 - 88.5
Sibanteng	90 – 91
Timbang	-
Sinila	70 – 71
Pagarkandang	91 – 92
Siglagah	90 – 92
Condrodimuko	84 – 85
Bitingan	63 – 64

Source : Volcano Observatory Office of Dieng Volcano

5.4.1 Standard TES Surface Temperature Anomaly

Standard LST extraction has been conducted in Dieng Volcano. The results is shown by the Figure 5.11 which is overlaid by DEM with 70% tranparancy. Temperatures in the volcano according to the three ASTER TIR scenes (2nd October 2005, 4th July 2007 and 6th July 2008) have range between 5°C to 25°C (Table 5.4). The average difference temperatures between images are between 0.6-1.76°C which image of 6th July 2008 shows highest different of average temperatatures. Atmosphere interference, long time sun shines, and/or local meteorological phenomenon which often occurs between mouths of July and August may affect lower average temperatures on 6th July 2008 (Weng & Fu 2014). The temperatures difference between images are constant within all of Dieng area which are not affected in temperature anomaly analysis.

The threshold of 95% confidence level is used to specify temperature anomaly, which is considered higher than average temperature in Dieng area (Table 5.4). The temperature anomaly in area of Dieng volcano was shown only by the large craters and dead lakes. The maximum temperatures in the three images were 25.94°C, 25.34°C and 21.73°C respectively, in the Sileri crater(Figure 5.11.b.c.d). Even though Sileri crater has the lowest temperature in the crater compared to the other craters, the size of the crater coupled with lake make the crater as the highest temperature in the images. Inactive crater lakes such as Telaga Warna, and Merdada also shown temperature anomalies, which caused by lakes water needing more time to cool down at night than surrounding land. The temperature anomaly in the outside of the Dieng volcano such as in the Northern part of study area are caused by the morphology difference between Dieng volcano and outside areas. The Northern part of study area is located in the open area which allows longer solar radiation. The wind exchange is also influenced by the warm air temperature blowing from the North coast area. Moreover, the threshold value is calculated only from the temperature in the Dieng area which has lower average temperature than outside area.

Small craters which have no lake such as Sikidang, Timbang, Wanapria, Pagarkandang and Condrodimukodo not show temperatures anomaly. Those craters have normal temperatures background between 12.65-15.30^{o}C. Thermal manifestation from these craters are not strong enough to be captured by the sensor. The possible cause is because the size of the craters is too small. Another possible cause is the position of the craters in terrain with undulating to steep slope. Altitude and slope effects could be the reasons why these craters' anomalies are not visible in the standard LST product (Ulusoy et al. 2012).

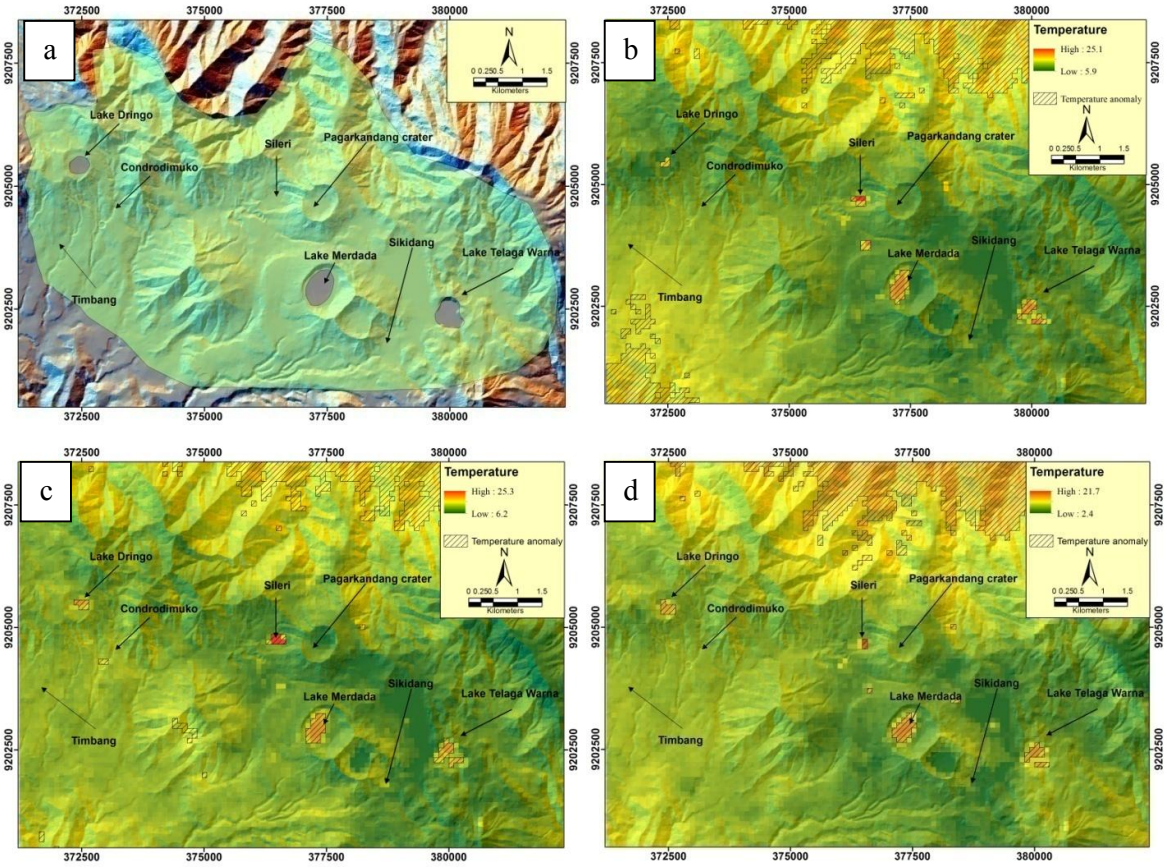

Figure 5.11. Hill-shade map of Dieng volcano and TES of three scenes ASTER Night Time TIR (a. Hillshade map which shows masked area for statistic calculation, b. 2nd October 2005, c. 4th July 2007 and d. 6th July 2008).

Table 5.4. Simple statistic parameters of original temperatures. (Threshold for temperature anomaly has 95% confidence level).

Date	Sub-map	Min (^{o}C)	Max (^{o}C)	Mean (^{o}C)	Stdev (^{o}C)	# of Pixels	Threshold
2nd October 2005	Dieng	5.99	25.12	13.41	1.42	6,121	16.25
	Sikidang	10.28	14.14	12.70	0.98	41	
	Sileri	12.32	25.94	14.40	2.95	35	
	Timbang	13.78	15.30	14.50	0.33	45	
4thJuly 2007	Dieng	6.25	25.34	12.79	1.33	6,121	15.45
	Sikidang	10.33	14.55	12.55	1.16	41	
	Sileri	11.40	25.34	13.92	3.99	35	
	Timbang	13.28	14.23	13.78	0.26	45	
6thJuly 2008	Dieng	2.61	21.74	10.94	1.89	6,121	14.72
	Sikidang	5.19	11.87	9.22	1.64	41	
	Sileri	8.61	21.74	11.04	2.60	35	
	Timbang	10.81	12.65	11.76	0.43	45	

5.4.2 Topographic Corrected Surface Temperature Anomaly

Topographic condition of Dieng volcano is undulating to steep slope, which could affect the temperature anomaly detection. Therefore, the result of temperature map needs a correction. The correction is based on the IDL code to normalize the lapse rate and illumination effects (Ulusoy et al. 2012). It uses Digital Elevation Model (DEM) from SRTM which has the same 90x90 m spatial resolution with the temperature map. From the SRTM DEM, slope and aspect are derived. The three parameter are in advance used to correct the temperature map. Masking procedure using the area as shown in Figure 5.11.a was used to avoid the topographic effects of the area outside study area as described by Ulusoy et al. (2012).

The scater plots in Figure 5.12 shows a negative linear correlation between temperature and altitude where the high temperature correlates with low altitude. It means that the altitude affects the temperature. Outliers to this relationship can be observed in the higher altitudes, between 2000 to 2500 meters. This affects large area in the North West parts such as lake Dringo area and South East parts of study area such as Sikidang crater and Telaga Warna lake areas. The

possitive anomalies (red dashed ovals) are caused by the cretar and lake effects, meanwhile negative anomalies (orange dashed ovals) can be affected by meteorological phenomenon such as katabatic flow which is also shown when applying same procedure in Mt. Nemrut volcano in Turkey (Ulusoy et al. 2012). As expected, the image of 6th July 2008 showed more temperature inversions which are affected by meteorological phenomenon.

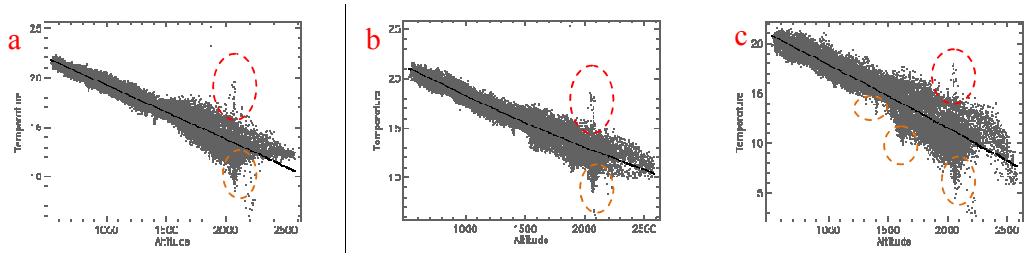

Figure 5.12. The correlation between temperature and altitude from three images (a. 2nd October 2005, b. 4th July 2007 and c. 6th July 2008).

The second correction is used aspect. The scater plot in Figure 5.13 shows the relationship between temperature and aspect. The three images use different fitting polynomial. The image of 2nd October 2005 and 4th July 2007 use second order of polynomial. Whereas, the image of 6th July 2008 represents higher distortion, therefore it needs 6th order of polynomial.

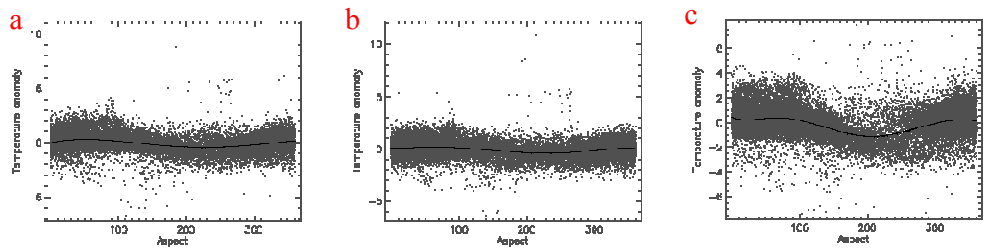

Figure 5.13. The correlation between temperature and aspect from three images (a. 2nd October 2005, b. 4th July 2007 and c. 6th July 2008).

The last step is the slope correction. The slope correction corrects the corrected altitude and aspect temperature images. The images of 2nd October 2005 and 6th July 2008 used 1st order polynomial while the 4th July 2007 use 2nd order polynomial. The temperature anomalies show deviations in relation with the increasing of the slope values Figure 5.14.

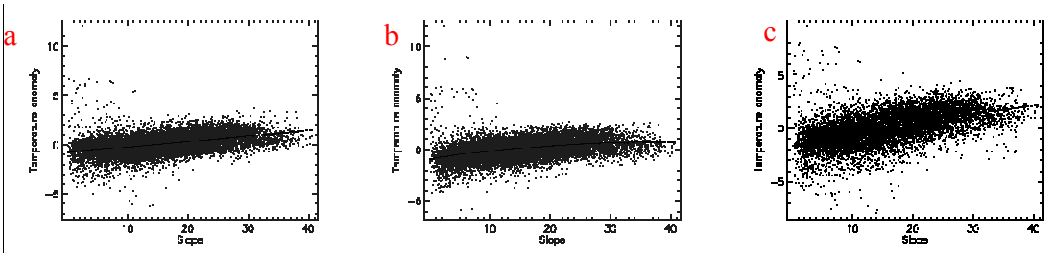

Figure 5.14. The correlation between temperature and slope from three images (a. 2nd October 2005, b. 4th July 2007 and c. 6th July 2008).

The three corrected temperature images show significance improvement of the temperature anomaly from the original LST images especially in the image of 4th July 2007. Simple statistic analysis of whole and certain parts of images (Table 5.5) represent the increasing temperatures in certain craters and hot spot of study area. The temperature anomaly now can be seen on the area of Sikidang crater as shown by contrast color and black dush lines of 95% confidence level of threshold in Figure 5.15. The whole standar deviation (Table 5.5) are also reduced compared with original temperature images (Table 5.4). However, there are no effect for some extents of craters especially for small craters such as Timbang and Pagarkandang. This indicates that the high temperatures of small craters can not affect the temperatures of surronding area, therefore the ASTER TIR sensor will obtain temperatures in the area as normal temperatures. Some topographic effects appear on the North part of the study area which generate temperature anomaly in the area. Some small dot of temperatus anomaly also apper in the study area outside the craters area (blue dash). They are correlated with geothermal activities in that area.

In the case of monitoring, temperature anomaly monitoring is potential to be used in two craters areas of Dieng volcano (Sileri and Sikidang) for phreatic eruption and toxic gases outburst events. The craters show significant temperature anomaly which can be observed by looking the temperature changes. However, ASTER with 16 days periodical data is only capable to provide monthly data which is only useful for long-term analysis. While, in the case of Dieng volcano with short period of toxic gases outbursts events and phreatic eruptions (Guern et al. 1982), it also need daily data to observe each change in the

temperature of the craters. Therefore, another procedure such as FTIR camera (Www.usgs.gov & IRIS n.d.) which mounted in an approriated can be applied to measure daily temperature. This procedure also can provide an understanding about different temperatures between normal condition and unrest volcanic events that can not be solved in this study.

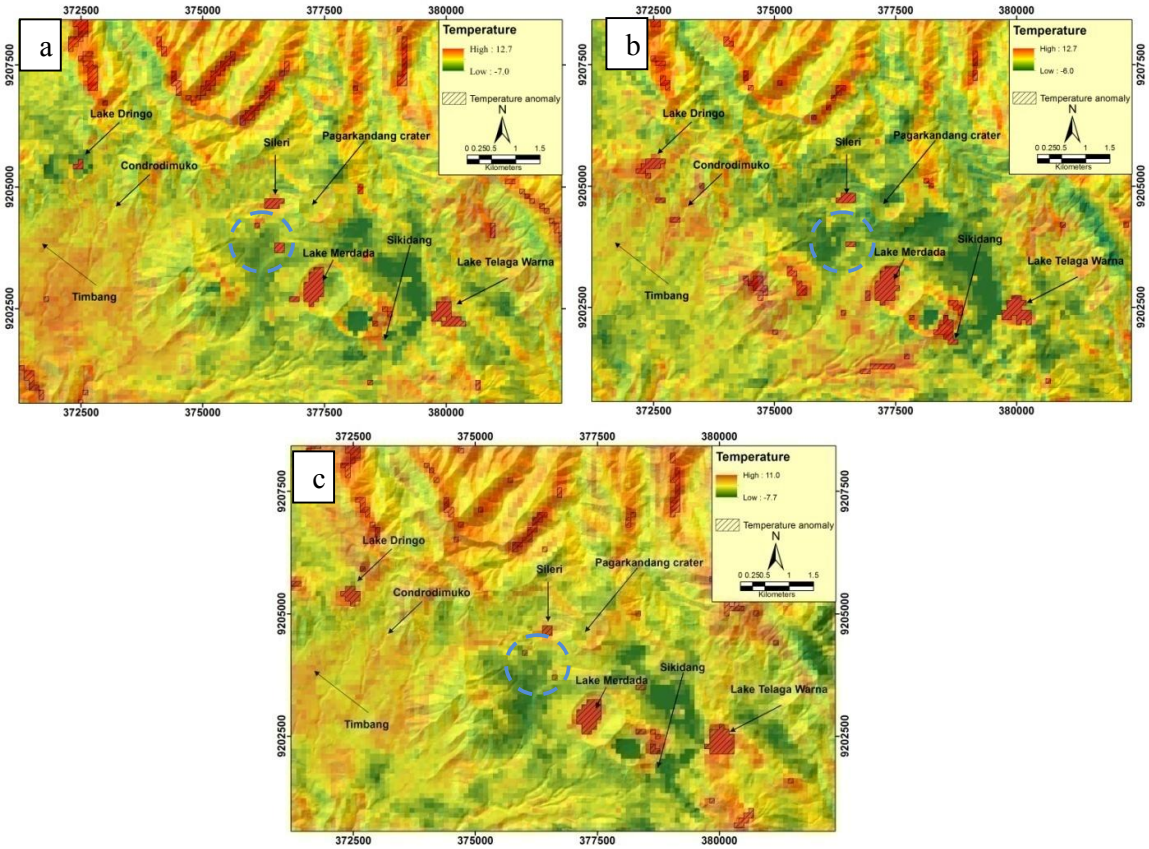

Figure 5.15. The topography-corrected temperature map of three LST images of ASTER Nighttime TIR (a. 2nd October 2005, b. 4th July 2007 and c. 6th July 2008).

Table 5.5. Simple statistic parameters of altitude and aspect corrected temperature. (Threshold for temperature anomaly has 95% confidence level).

Date	Sub-map	Min (oC)	Max (oC)	Mean (oC)	Stdev (oC)	# of Pixels	Threshold
2nd October 2005	Whole	-7.04	12.76	-0.34	1.00	6,121	1.66
	Sikidang	-2.86	2.02	-0.02	1.29	41	
	Sileri	-1.15	12.76	0.98	3.03	35	
	Timbang	-0.82	0.77	0.16	0.40	45	
4th July 2007	Whole	-6.08	12.77	-0.30	0.97	-6.08	1.63
	Sikidang	-2.07	2.82	0.42	1.50	41	
	Sileri	-1.45	12.87	1.17	4.07	35	
	Timbang	-0.55	0.79	0.09	0.31	45	
6th July 2008	Whole	-7.67	11.01	-0.23	1.35	6,121	2.46
	Sikidang	-5.13	2.68	-1.09	2.05	41	
	Sileri	-1.79	11.01	0.71	2.68	35	
	Timbang	-0.76	1.64	0.48	0.48	45	

Chapter 6. Conclussion and Recommendation

6.1 Conclussion

Based on the presented results, the following conclusion can be drawn:

1. Sikidang and Sileri craters represent the characteristic of craters in East part of Dieng volcano which are multi-fractures and large area. The Sikidang releases SO_2 (0 – 126.1 ppm), H_2S (0.6 – 66 ppm), and CO_2 (0 – 2% mol.) from several fractures in the area. While Sileri crater emits SO_2 (0.4 – 10.1 ppm), H_2S (0.5 – 5 ppm) and CO_2 (0 - 0.3 % mol.) mainly from its main crater lake. In contrast, the craters in the West part of Dieng volcano are represented by single fracture and narrow craters such as Timbang and Conrodimuko craters. The single fracture of Condrodimuko crater releases 2 – 9.9 ppm SO_2, 1 – 6.1 ppm H_2S and 0 – 0.3 % mol CO_2 which is almost similar values with Sileri crater.
2. The fault analysis results in 4 faults (L1, L2, L3 and L4). The epicenters of local tectonic earthquakes are mostly located in the middle part of study area within the zone of West part craters and associated with L3 and L4 faults. VTA earthquakes also overlay middle part of study area and concuring with L2 fault. However, the VTB earthquakes are not coinciding with any faults. The three faults of L1, L2 and L3 correlate with craters in West part area such as Timbang, Condrodimuka, Wanapriya and Sinila which form a complex fault system. One fault (L4) corresponds with craters in East zone such as Sileri, Sikidang, Sibanteng, Siglagah, Bitingan, Sikendang, Pakuwojo, and Pagarkandang.
3. The three cyclical periods of seismic features (local tectonic, VTA and VTB earthquakes) have shown no correlation with the time lag between two toxic gases outburst events and phreatic eruption. The local tectonic, VTA, and VTB earthquakes have 153.6 days, 288 days and 460.8 days of cyclical periods respectively. While, the time lags between two toxic gases outbursts events and phreatic eruption are between 600 - 650 days.

4. The graph analysis of magnitude and frequency of long-term seismic features data (local tectonic, VTA and VTB earthquakes) shows that toxic gases outburst events have a high correlation with the strong magnitude of local tectonic earthquakes and high frequency of seismic features. Meanwhile, the phreatic eruption in Sileri crater which occurred in 2009 has no correlation either with seismic events (the strong magnitude of local tectonic earthquakes or high seismic frequency) or toxic gases outburst events.
5. The CCF analysis of long-term seismic events data (local tectonic, VTA and VTB earthquakes) shows the dominant influence of local tectonic earthquakes to VTA events. The influence is indicated by the high correlation between them with the highest correlation value 64.3 % that occur in 0 lag and the correlation tend to occur in positive lags. While, the influence of local tectonic to VTB events are less which is shown by the lower correlation between them (35.5%). VTB events are more influenced by VTA event which is shown by high correlations value (69.2%) which occur in 0 and continues high in positive lags.The CCF analysis is consistent with the cyclical pattern analysis. The high correlation is corresponding with the nearest cyclical period of the seismic events. Furthermore, it shows a good agreement with the spatial fault analysis.
6. The cross correlation analysis of short-term single toxic gases outburst event shows the delay times and duration of the seismic events prior to the toxic gases outburst event. The graph analysis shows that the peak frequency of local tectonic and VTA earthquakes have 1-2 days of delay times and peak frequency of VTB earthquake has 8 days delay times to the event of toxic gases outburst. The CCF analysis shows inverse correlations between seismic events and CO_2 gases emission which show the duration of toxic gases outburst events. The maximum duration of toxic gases outburst event in the relation with peak frequency of local tectonic and VTA earthquakes are 7 and 5 days respectively. However, the CCF calculation for VTB earthquake has shows an error due to the longer delay

times between peak frequency of VTB earthquake and the event of toxic gases outburst.

7. The first step of SO_2 retrieval failed to visually highlight an SO_2 plume. This affects to the the next steps of SO_2 retrieval which can not be continued. The concentration of SO_2 in the study area appears to below the detection limit of the ASTER TIR method.
8. The original temperature extraction from ASTER TIR images shows anomaly in craters with lakes, however it is not clear for the crater without lake and for small crater. The highest temperature is manifested by the Sileri crater and the lowest temperature by the Timbang crater. Inactive crater lakes also give false positive anomalies due to higher thermal inertia.
9. The topography-corrected temperature shows an improvement from the original temperature images which reveal temperature anomalies for large craters without lake such as Sikidang. However, it can not be revealed the temperature anomaly for small crates such as Timbang and Pagarkandang.

6.2 Recommendation

1. The emphasizing of the volcanic monitoring in Dieng volcano should be on the VTB event which has longer delay time before the eruption occurs. Moreover, the local tectonic earthquake with magnitude higher than 3.5 Richter scales should also be concerned.
2. Temperature monitoring can be an alternative in Dieng volcano especially to fulfill the weakness of the seismic monitoring in identifying the indication of phreatic eruption in Sileri crater. However, further research is required to explore the different temperature between normal condition and unrest volcanic events.

References:

Abidin, H.Z. et al., 2007. Volcano Deformation Monitoring in Indonesia : Status , Limitations and Prospects.

Al-amri, S.S., Kalyankar, N. V & Khamitkar, S.D., 2010. Linear and Non-linear Contrast Enhancement Image. *Journal of Computer Science*, 10(2), pp.139–143. Available at: http://paper.ijcsns.org/07_book/201002/20100222.pdf.

Allard, P., Dajlevic, D. & Delarue, C., 1989. Origin of carbon dioxide emanation from the 1979 Dieng eruption, Indonesia: Implications for the origin of the 1986 Nyos catastrophe. *Journal of Volcanology and Geothermal Research*, 39(2-3), pp.195–206. Available at: http://linkinghub.elsevier.com/retrieve/pii/0377027389900589.

Arbangiyah, R., 2012. *Perubahan Pola Pertanian Raykat di desa Sembungan Dataran Tinggi Dieng (1985-1995)/ The changed pattern in smallholder agriculture of Sembungan village of Dieng Plateau (1985-1995)*. University of Indonesia.

Arun, P.V., 2013. A comparative analysis of different DEM interpolation methods. *The Egyptian Journal of Remote Sensing and Space Science*, 16(2), pp.133–139. Available at: http://www.sciencedirect.com/science/article/pii/S1110982313000276.

Barry, P.H. et al., 2014. Carbon isotope and abundance systematics of Icelandic geothermal gases, fluids and subglacial basalts with implications for mantle plume-related CO2 fluxes. *Geochimica et Cosmochimica Acta*, 134, pp.74–99. Available at: http://linkinghub.elsevier.com/retrieve/pii/S0016703714001471 [Accessed June 2, 2014].

Baxter, P. eter J. & Kapila, M., 1989. Acute health impact of the gas release at Lake Nyos , Cameroon , 1986. , 39, pp.265–275.

Bonetto, S. et al., 2015. A tool for semi-automatic linear feature detection based on DTM. *Computers & Geosciences*, 75, pp.1–12. Available at: http://linkinghub.elsevier.com/retrieve/pii/S0098300414002283.

Bruno, N. et al., 2001. Degassing of SO 2 and CO 2 at Mount Etna (Sicily) as an indicator of pre-eruptive ascent and shallow emplacement of magma. , 110.

Budi-santoso, A. et al., 2013. Analysis of the seismic activity associated with the 2010 eruption of Merapi Volcano , Java. *Journal of Volcanology and Geothermal Research*, 261(November 2010), pp.153–170. Available at: http://dx.doi.org/10.1016/j.jvolgeores.2013.03.024.

Campion, R. et al., 2010. Measuring volcanic degassing of SO2 in the lower troposphere with ASTER band ratios. *Journal of Volcanology and Geothermal Research*, 194(1-3), pp.42–54. Available at: http://linkinghub.elsevier.com/retrieve/pii/S0377027310001289 [Accessed June 2, 2014].

Carlos, J., Munoz, J. & Sabrino, J.A., 2008. Split-Window Coefficients for Land Surface Temperature Retrieval From Low-Resolution Thermal Infrared Sensors. *IEEE Geoscince and Remote Sensing Letters*, 5(4), pp.806–809.

Carter, A.J. et al., 2008. ASTER and field observations of the 24 December 2006 eruption of Bezymianny Volcano, Russia. *Remote Sensing of Environment*, 112(5), pp.2569–2577. Available at: http://ezproxy.utwente.nl:2105/CitedFullRecord.do?product=WOS&colName=WOS&SID=Y1H9raDlB5dNRhRS4eh&search_mode=CitedFullRecord&isickref=WOS:000255370700049 [Accessed May 6, 2014].

Chen, M. & Chen, B., 2014. Online fuzzy time series analysis based on entropy discretization and a Fast Fourier Transform. *Applied Soft Computing*, 14, pp.156–166. Available at: http://www.sciencedirect.com/science/article/pii/S1568494613002780.

Cheng, J. et al., 2008. Correlation-based temperature and emissivity separation algorithm. *Science in China Series D: Earth Sciences*, 51(3), pp.357–369. Available at: http://link.springer.com/10.1007/s11430-008-0022-7 [Accessed May 27, 2014].

Coll, C. et al., 2007. Temperature and emissivity separation from ASTER data for low spectral contrast surfaces. *Remote Sensing of Environment*, 110, pp.162–175.

Cowpertwait, P.S.P. & Metcalfe, A. V., 2011. *Introductory Time Series with R*,

Davies, R. et al., 2007. Cloud motion vectors from MISR using sub-pixel enhancements. *Remote Sensing of Environment*, 107(1-2), pp.194–199.

DiStasio, R.J. & Resmini, R.G., 2010. Atmospheric compensation of thermal infrared hyperspectral imagery with the emissive empirical line method and the in-scene atmospheric compensation algortihms: A comparison S. S. Shen & P. E. Lewis, eds. *Society of Photo-Optical Instrumentation Engineers*, p.76952B–76952B–12. Available at: http://proceedings.spiedigitallibrary.org/proceeding.aspx?articleid=1345005.

Evrendilek, F. et al., 2012. Satellite-based and mesoscale regression modeling of monthly air and soil temperatures over complex terrain in Turkey. *Expert Systems with Applications*, 39(2), pp.2059–2066. Available at: http://dx.doi.org/10.1016/j.eswa.2011.08.023.

Frondini, F. et al., 2009. Carbon dioxide degassing and thermal energy release in the Monte Amiata volcanic-geothermal area (Italy). *Applied Geochemistry*, 24(5), pp.860–875. Available at: http://linkinghub.elsevier.com/retrieve/pii/S0883292709000286 [Accessed July 31, 2014].

Gallant, J.C. & Hutchinson, M.F., 1997. Scale dependence in terrain analysis. *Mathematics and Computers in Simulation*, 43, pp.313–321.

Geological Agency of Indonesia, P., Basic data of volcano; Dieng. , pp.1–7. Available at: http://www.vsi.esdm.go.id/index.php/gunungapi/data-dasar-gunungapi/531-g-dieng?start=5.

Giggenbach, W.E., Sano, Y. & Schmincke, H.U., 1991. CO2-rich gases from Lakes Nyos and Monoun , Cameroon ; Laacher See , Germany ; Dieng , Indonesia , and Mt . Gambier , Australia variations on a common theme. , 45, pp.311–323.

Gillespie, a. et al., 1998. A temperature and emissivity separation algorithm for Advanced Spaceborne Thermal Emission and Reflection Radiometer (ASTER) images. *IEEE Transactions on Geoscience and Remote Sensing*,

36(4), pp.1113–1126. Available at: http://ieeexplore.ieee.org/lpdocs/epic03/wrapper.htm?arnumber=700995.

Gillespie, A.R. et al., 2011. Residual errors in ASTER temperature and emissivity standard products AST08 and AST05. *Remote Sensing of Environment*, 115(12), pp.3681–3694. Available at: http://dx.doi.org/10.1016/j.rse.2011.09.007.

Guern, F.L.E., Tazieff, H. & Pierret, R.F., 1982. An Example of Health Hazard: People Killed by Gas during a Phreatic Eruption: Dieng Plateau (Java, Indonesia), February 20th 1979. *Bulletin of Volcanology*, 45, pp.2–5.

Hashim, M. et al., 2013. Automatic lineament extraction in a heavily vegetated region using Landsat Enhanced Thematic Mapper (ETM +) imagery. *Advances in Space Research*, 51(5), pp.874–890. Available at: http://dx.doi.org/10.1016/j.asr.2012.10.004.

Jacob, F. et al., 2004. Comparison of land surface emissivity and radiometric temperature derived from MODIS and ASTER sensors. *Remote Sensing of Environment*, 90(2), pp.137–152. Available at: http://linkinghub.elsevier.com/retrieve/pii/S0034425703003699 [Accessed July 15, 2014].

Jordan, G. et al., 2005. Extraction of morphotectonic features from DEMs: Development and applications for study areas in Hungary and NW Greece. *International Journal of Applied Earth Observation and Geoinformation*, 7, pp.163–182.

Jordan, G. & Schott, B., 2005. Application of wavelet analysis to the study of spatial pattern of morphotectonic lineaments in digital terrain models. A case study. *Remote Sensing of Environment*, 94, pp.31–38.

Jousset, P. et al., 2013. Signs of magma ascent in LP and VLP seismic events and link to degassing : An example from the 2010 explosive eruption at Merapi volcano , Indonesia. *Journal of Volcanology and Geothermal Research*, 261, pp.171–192. Available at: http://dx.doi.org/10.1016/j.jvolgeores.2013.03.014.

Jousset, P. et al., 2012. The 2010 explosive eruption of Java's Merapi volcano—A "100-year" event. *Journal of Volcanology and Geothermal Research*, 241-242, pp.121–135. Available at: http://linkinghub.elsevier.com/retrieve/pii/S0377027312001862 [Accessed May 24, 2014].

Jousset, P. & Pallister, J., 2013. The 2010 eruption of Merapi volcano. *Journal of Volcanology and Geothermal Research*, 261, pp.1–6. Available at: http://linkinghub.elsevier.com/retrieve/pii/S0377027313001492 [Accessed May 26, 2014].

Kalacheva, E., Taran, Y. & Kotenko, T., 2015. Geochemistry and solute fluxes of volcano-hydrothermal systems of Shiashkotan, Kuril Islands. *Journal of Volcanology and Geothermal Research*, 296, pp.40–54. Available at: http://linkinghub.elsevier.com/retrieve/pii/S0377027315000761.

Katili, J.A., 1974. Volcanism and Plate Tectonics in the Indonesian Island Arcs. *Tectonophysiscs*, 26(Elsevier Scientific Publishing Company, Amsterdam), pp.165–188.

Kondo, K., Tsuchiya, M. & Sanada, S., 2002. Evaluation of effect of micro-topography on design wind velocity. *Journal of Wind Engineering and Industrial Aerodynamics*, 90(12-15), pp.1707–1718.

Lagios, E. et al., 2007. Testing satellite and ground thermal imaging of low-temperature fumarolic fields : The dormant Nisyros Volcano (Greece). , 62, pp.447–460.

Lamb, O.D. et al., 2014. Similar cyclic behaviour observed at two lava domes, Volcán de Colima (Mexico) and Soufrière Hills volcano (Montserrat), with implications for monitoring. *Journal of Volcanology and Geothermal Research*. Available at: http://linkinghub.elsevier.com/retrieve/pii/S0377027314002261 [Accessed August 11, 2014].

Li, Z.-L. et al., 2013. Satellite-derived land surface temperature: Current status and perspectives. *Remote Sensing of Environment*, 131, pp.14–37. Available at:http://linkinghub.elsevier.com/retrieve/pii/S0034425712004749 [Accessed May 25, 2014].

Matthews, A.J., Barclay, J. & Johnstone, J.E., 2009. The fast response of volcano-seismic activity to intense precipitation: Triggering of primary volcanic activity by rainfall at Soufrière Hills Volcano, Montserrat. *Journal of Volcanology and Geothermal Research*, 184(3-4), pp.405–415. Available at: http://linkinghub.elsevier.com/retrieve/pii/S0377027309002261 [Accessed August 25, 2014].

Mayaud, C. et al., 2014. Single event time series analysis in a binary karst catchment evaluated using a groundwater model (Lurbach system, Austria). *Journal of Hydrology*, 511, pp.628–639. Available at: http://dx.doi.org/10.1016/j.jhydrol.2014.02.024.

Van der Meer, F. et al., 2014. Geologic remote sensing for geothermal exploration: A review. *International Journal of Applied Earth Observation and Geoinformation*, 33, pp.255–269. Available at: http://linkinghub. elsevier.com/ retrieve/pii/S0303243414001275 [Accessed July 20, 2014].

Miller, C.D. et al., 1983. Eruptive history of the Dieng Mountains Region, Central Java, and Potential Hazards from future eruptions. *United State Departement of the Interior Geological Survey*, 83-68(Open-File Report).

Nicholson, E.J. et al., 2013. Cyclical patterns in volcanic degassing revealed by SO2 flux timeseries analysis: An application to Soufrière Hills Volcano, Montserrat. *Earth and Planetary Science Letters*, 375, pp.209–221. Available at: http://linkinghub.elsevier.com/retrieve/pii/S0012821X1300277X [Accessed July 15, 2014].

Olmos, R. et al., 2007. Anomalous Emissions of SO2 During the Recent Eruption of Santa Ana Volcano, El Salvador, Central America. *Pure and Applied Geophysics*, 164(12), pp.2489–2506. Available at: http://link.springer.com/ 10.1007/s00024-007-0276-6 [Accessed August 19, 2014].

Pacey, A., Macpherson, C.G. & McCaffrey, K.J.W., 2013. Linear volcanic segments in the central Sunda Arc, Indonesia, identified using Hough Transform analysis: Implications for arc lithosphere control upon volcano distribution. *Earth and Planetary Science Letters*, 369-370, pp.24–33. Available at:

http://linkinghub.elsevier.com/retrieve/pii/S0012821X13001155 [Accessed June 3, 2014].

Peng, C.K. et al., 1994. Mosaic organization of DNA nucleotides. *Physical Review E*, 49(2), pp.1685–1689.

Pieri, D. & Abrams, M., 2004. ASTER watches the world's volcanoes: a new paradigm for volcanological observations from orbit. *Journal of Volcanology and Geothermal Research*, 135(1-2), pp.13–28. Available at: http://linkinghub.elsevier.com/retrieve/pii/S0377027304000277 [Accessed July 25, 2014].

Pugnaghi, S. et al., 2006. Mt. Etna sulfur dioxide flux monitoring using ASTER-TIR data and atmospheric observations. *Journal of Volcanology and Geothermal Research*, 152(1-2), pp.74–90. Available at: http://linkinghub.elsevier.com/retrieve/pii/S037702730500346X [Accessed June 2, 2014].

Ramsey, M. & Dehn, J., 2004. Spaceborne observations of the 2000 Bezymianny, Kamchatka eruption: the integration of high-resolution ASTER data into near real-time monitoring using AVHRR. *Journal of Volcanology and Geothermal Research*, 135(1-2), pp.127–146. Available at: http://linkinghub.elsevier.com/retrieve/pii/S0377027304000332 [Accessed June 2, 2014].

Ramsey, M.S. & Harris, A.J.L., 2013. Volcanology 2020: How will thermal remote sensing of volcanic surface activity evolve over the next decade? *Journal of Volcanology and Geothermal Research*, 249, pp.217–233. Available at: http://www.sciencedirect.com/science/article/pii/S0377027312001497 [Accessed May 25, 2014].

Realmuto, V.J. & Worden, H.M., 2000. Impact of atmospheric water vapor on the thermal infrared remote sensing of volcanic sulfur dioxide emissions: A case study from the Pu'u "O"o vent of Kilauea Volcano, Hawaii. *Journal of Geophysical Research*, 105(B9), p.21497.

Rossiter, D.G., 2012. *Time series analysis in R*, Version 1.0. Copyright 2009–2012 D G Rossiter. Available at: (http://www.itc.nl/personal/rossiter).

Sabol, Jr., D.E. et al., 2009. Field validation of the ASTER Temperature–Emissivity Separation algorithm. *Remote Sensing of Environment*, 113(11), pp.2328–2344. Available at: http://linkinghub.elsevier.com/retrieve/pii/S0034425709001898 [Accessed August 13, 2014].

Soto-pinto, C., Arellano-baeza, A. & Sánchez, G., 2013. A new code for automatic detection and analysis of the lineament patterns for geophysical and geological purposes (ADALGEO). *Computers and Geosciences*, 57, pp.93–103. Available at: http://dx.doi.org/10.1016/j.cageo.2013.03.019.

Spampinato, L. et al., 2011. Volcano surveillance using infrared cameras. *Earth-Science Reviews*, 106(1-2), pp.63–91. Available at: http://linkinghub.elsevier.com/ retrieve/pii/S0012825211000043 [Accessed May 25, 2014].

Sukamar, M., Venkatesan, N. & Babu, C.N.K., 2014. A Review of Various Lineament Detection Techniques for high resolution Satellite Images. *International Journal of Advanced Research in Computer Science and Software Engineering*, 4(3), pp.72–78. Available at:

http://www.ijarcsse.com/docs/papers/Special_Issue/icctrd2014/ijarcsse_022.pdf.

Trunk, L. & Bernard, A., 2008. Investigating crater lake warming using ASTER thermal imagery: Case studies at Ruapehu, Poás, Kawah Ijen, and Copahué Volcanoes. *Journal of Volcanology and Geothermal Research*, 178(2), pp.259–270. Available at: http://linkinghub.elsevier.com/retrieve/pii/S0377027308003600 [Accessed May 25, 2014].

Ulusoy, I., Labazuy, P. & Aydar, E., 2012. STcorr : An IDL code for image based normalization of lapse rate and illumination effects on nighttime TIR imagery. , 43, pp.63–72.

Urai, M., 2004. Sulfur dioxide flux estimation from volcanoes using Advanced Spaceborne Thermal Emission and Reflection Radiometer—a case study of Miyakejima volcano, Japan. *Journal of Volcanology and Geothermal Research*, 134(1-2), pp.1–13. Available at: http://linkinghub.elsevier.com/retrieve/ pii/S0377027303004153 [Accessed August 13, 2014].

USGS, V.H.P., Measuring volcanic gases: emission rates of sulfur dioxide and carbon dioxide in volcanic plumes. Available at: http://volcanoes.usgs.gov/activity/methods/gas/plumes.php [Accessed January 9, 2015].

Vaughan, R.G. et al., 2010. Exploring the limits of identifying sub-pixel thermal features using ASTER TIR data. *Journal of Volcanology and Geothermal Research*, 189(3-4), pp.225–237. Available at: http://linkinghub.elsevier.com/ retrieve/pii/S0377027309004429 [Accessed June 2, 2014].

Vaughan, R.G. et al., 2005. Monitoring eruptive activity at Mount St. Helens with TIR image data. *Geophysical Research Letters*, 32(19), p.L19305. Available at: http://doi.wiley.com/10.1029/2005GL024112 [Accessed May 24, 2014].

Vaughan, R.G. et al., 2012. Use of ASTER and MODIS thermal infrared data to quantify heat fl ow and hydrothermal change at Yellowstone National Park. *Journal of Volcanology and Geothermal Research*, 233-234, pp.72–89. Available at: http://dx.doi.org/10.1016/j.jvolgeores.2012.04.022.

Watson, I.. et al., 2004. Thermal infrared remote sensing of volcanic emissions using the moderate resolution imaging spectroradiometer. *Journal of Volcanology and Geothermal Research*, 135(1-2), pp.75–89. Available at: http://www.sciencedirect.com/science/article/pii/S0377027304000307 [Accessed May 21, 2014].

Weng, Q. & Fu, P., 2014. Remote Sensing of Environment Modeling annual parameters of clear-sky land surface temperature variations and evaluating the impact of cloud cover using time series of Landsat TIR data. *Remote Sensing of Environment*, 140, pp.267–278. Available at: http://dx.doi.org/10.1016/j.rse.2013.09.002.

Werner, C. et al., 2013. Degassing of CO2, SO2, and H2S associated with the 2009 eruption of Redoubt Volcano, Alaska. *Journal of Volcanology and Geothermal Research*, 259, pp.270–284. Available at: http://linkinghub.elsevier.com/retrieve/pii/S0377027312000996 [Accessed July 30, 2014].

Www.usgs.gov & IRIS, Volcano Monitoring : Deformation , Seismicity & Gas. Available at: http://volcanoes.usgs.gov/activity/methods/index.php.

Yamaguchi, Y. et al., 1998. Overview of Advanced Spaceborne Thermal Emission and Reflection Radiometer (ASTER). *IEEE Transactions on Geoscience and Remote Sensing*, 36(4), pp.1062–1071. Available at: http://ieeexplore.ieee.org/lpdocs/epic03/wrapper.htm?arnumber=700991.

Zielke, O., Klinger, Y. & Arrowsmith, J.R., 2015. Fault slip and earthquake recurrence along strike-slip faults — Contributions of high-resolution geomorphic data. *Tectonophysics*, 638, pp.43–62. Available at: http://dx.doi.org/10.1016/j.tecto.2014.11.004.

Zlotnicki, J. et al., 2000. Magnetic monitoring at Merapi volcano , Indonesia. , 100, pp.321–336.

Appendix 1. Mobile Gases Measurement

1. The gases measurement in night of 2nd October 2014

Condrodimuko I		7°11,348'	109°51,210'		
Time start	20.14				
Gases	I	II	III	IV	V
CO_2	0	0	0	0	0
SO_2	2.5	5	3.3	2.7	3.2
H_2S	1	2.1	2	1.7	1.8
Condrodimuko II					
Time start	20.24				
Gases	I	II	III	IV	V
CO_2	0	0	0	0	0
SO_2	7.6	8.1	9.9	9.5	9
H_2S	2	4.1	6.1	5.3	2
Sileri I	109.8839	-7.19347			
Time start	21.04				
Gases	I	II	III	IV	V
CO_2	0	0	0	0	0
SO_2	2	2.1	3.2	2.5	3
H_2S	0	0	0	0	0
Sileri II					
Time start	21.18				
Gases	I	II	III	IV	V
CO_2	0	0	0	0	0
SO_2	2.4	2.5	2.1	3	2.5
H_2S	0	0	0	0	0
Sileri III					
Time start	21.27				
Gases	I	II	III	IV	V
CO_2	0	0	0	0	0
SO_2	2.2	2.5	2.8	2.1	2.7
H_2S	0	0	0	0	0
Sileri IV					
Time start	21.35				
Gases	I	II	III	IV	V
CO_2	0	0	0	0	0
SO_2	2.3	2.6	2.3	2.1	2.8
H_2S	0	0	0	0	0

Sikidang I	109.904	-7.22042			
Time start	21.55				
Gases	I	II	III	IV	V
CO_2	0	0	0	0	0
SO_2	10	11.1	12.5	10.7	10.2
H_2S	1	2	3	2	2
Sikidang II					
Time start	22.03				
Gases	I	II	III	IV	V
CO_2	0	0	0	0	0
SO_2	8.4	8.7	9.1	8.1	8.1
H_2S	1	2	3	1	2
Sikidang III					
Time start	22.10				
Gases	I	II	III	IV	V
CO_2	0	0	0	0	0
SO_2	12.7	13.6	13.9	14.3	17.5
H_2S	3	2	4	7	9
Sikidang IIV					
Time start	22.13				
Gases	I	II	III	IV	V
CO_2	0	0	0	0	0
SO_2	> 20	> 20	> 20	> 20	> 20
H_2S	12	10	19	24	27
Sibanteng	109.903	-7.22005			
Time start	22.31				
Gases	I	II	III	IV	V
CO_2	0	0	0	0	0
SO_2	> 20	> 20	> 20	> 20	> 20
H_2S	40	45	63	51	69

Note : The measurement was taken 5 times in each location with time lag 1 minute. The SO_2 and H_2S in ppm and CO_2 in % mol..

2. The gases measurement on 9th October 2014

NO	Stasiun	X	Y	SO_2	H_2S
1	SK-1	109.9061	-7.21965	7.2	2.1
2	SK-2	109.9053	-7.2199	4.5	1.8
3	SK-3	109.9045	-7.22018	5.5	1.4
4	SK-4	109.9041	-7.22043	9.1	2.4
5	SK-5	109.9037	-7.22043	100	66
6	SK-6	109.9031	-7.22053	50	17.8
7	SK-7	109.9028	-7.22073	31	7.7
8	SK-8	109.9017	-7.22102	9.2	0.8
9	SK-9	109.9031	-7.22002	34	7.8
10	SK-10	109.9038	-7.22013	12	1.6
11	SK-11	109.9039	-7.21997	6.2	0
12	SK-12	109.9038	-7.21952	8.5	1.4
13	SK-13	109.9038	-7.21888	7	0.7
14	SK-14	109.9046	-7.21937	5.9	0.5
15	SK-15	109.9049	-7.22049	5.3	2.2
16	SK-16	109.9053	-7.22087	3.1	1.1
17	SL-1	109.8827	-7.19298	3.6	2.1
18	SL-2	109.883	-7.19288	7.2	2.3
19	SL-3	109.8835	-7.19212	7.5	2.6
20	SL-4	109.8846	-7.19208	1.3	0.7
21	SL-5	109.8848	-7.19292	9.8	3
22	SL-6	109.8841	-7.19352	1.8	0.9
23	SL-7	109.8827	-7.194	0.6	0.6

3. The gases measurement on 25th October 2014

NO	Stasiun	X	Y	SO_2	H_2S
1	SK-1	109.9061	-7.21965	9.1	1.9
2	SK-2	109.9053	-7.2199	3.1	1.1
3	SK-3	109.9045	-7.22018	6.7	2.1
4	SK-4	109.9041	-7.22043	15.1	5.8
5	SK-5	109.9037	-7.22043	94.1	40.1
6	SK-6	109.9031	-7.22053	31.1	9.8
7	SK-7	109.9028	-7.22073	18.1	6.8
8	SK-8	109.9017	-7.22102	6.5	2.1
9	SK-9	109.9031	-7.22002	56	15.7
10	SK-10	109.9038	-7.22013	9.8	3.1
11	SK-11	109.9039	-7.21997	6.1	1.5
12	SK-12	109.9038	-7.21952	7.1	2.3
13	SK-13	109.9038	-7.21888	4.7	1.1
14	SK-14	109.9046	-7.21937	4.4	1
15	SK-15	109.9049	-7.22049	3.1	1.2
16	SK-16	109.9053	-7.22087	4.5	1.1
17	SL-1	109.8827	-7.19298	4.7	1.6
18	SL-2	109.883	-7.19288	7.4	2.2
19	SL-3	109.8835	-7.19212	7.1	2.4
20	SL-4	109.8846	-7.19208	1.2	0.4
21	SL-5	109.8848	-7.19292	6.1	2.1
22	SL-6	109.8841	-7.19352	1.2	0
23	SL-7	109.8827	-7.194	0	0

Appendix 2. Geological structure measurement

Station	ST-01		
Location	Timbang		
Types	Stike (N…^{o}E)	Dip (^{o})	Direction
Net slip	97	24	175
Fault plane	175	89	
Fault plane	159	90	
Fault breccia			167
Joint	24	15	
Joint	98	70	
Joint	20	55	
Joint	12	69	
Joint	49	76	
Joint	12	69	
Station	ST-02		
Location	Sikidang		
Types	Stike (N…^{o}E)	Dip (^{o})	Direction
Joint	36	66	
Joint	109	64	
Joint	109	70	
Station	ST-03		
Location	Sileri		
Types	Stike (N…^{o}E)	Dip (^{o})	Direction
Fault plane	80	75	245
Station	ST-04		
Location	Sileri 1		
Types	Stike (N…^{o}E)	Dip (^{o})	Direction
Fault plane	60	70	
Fault plane	250	75	
Station	ST-06		
Location	Condrodimuko 1		
Types	Stike (N…^{o}E)	Dip (^{o})	Direction
Joint	325	71	
Joint	49	90	
Joint	150	89	
Station	ST-09		

Location	Condrodimuko 2		
Types	Stike (N…^{o}E)	Dip (^{o})	Direction
Joint	138	80	
Joint	120	65	
Joint	51	30	
Joint	356	70	
Station	ST-10		
Location	River		
Types	Stike (N…^{o}E)	Dip (^{o})	Direction
Fault breccia	354	41	
Joints	65	74	
Joints	145	55	
Joints	56	62	
Joints	34	63	
Joints	185	66	
Joints	101	81	
Joints	225	65	
Joints	186	39	
Joints	89	86	
Station	ST-11		
Location	Sileri 2		
Types	Stike (N…^{o}E)	Dip (^{o})	Direction
fault scraps			95
Station	ST-12		
Location	Pagarkandang		
Types	Stike (N…^{o}E)	Dip (^{o})	Direction
fault scraps			125
Station	ST-14		
Location	Sikunir		
Types	Stike (N…^{o}E)	Dip (^{o})	Direction
Joint	40	60	
Joint	60	46	
Joint	44	55	
Joint	60	70	
Joint	98	84	
Joint	202	68	
Joint	20	40	

Station	ST-15		
Location	Merdada		
Types	Stike (N…^{o}E)	Dip (^{o})	Direction
Fault plane	211	74	

Appendix 3. R Script for Time Series Analysis

Cyclical Pattern Analysis of Long-Term Seismic Data

```
sve=read.csv("Volcanic and tectonic earthquake.csv", header=T)
tl.ts <- ts(sve$TL) # time series of local tectonic earthquake
va.ts <- ts(sve$VA) # time series of deep volcanic earthquake
vb.ts <- ts(sve$VB) # time series of shallow volcanic earthquake
# spectral density of local tectonic earthquake
tl.sp <- spectrum(tl.ts, spans = c(5,7), taper =0.1, log = "yes", main = "Local
    Tectonic Earthquake",  sub= "Cycles/day, smoothed" )
tl.sp$freq[which.max(tl.sp$spec)] # to reveal the frequency domain of the highest
    spectrum
frequency(tl.ts)/(tl.sp$freq[which.max(tl.sp$spec)]) # to reveal the period of the
    highest spectrum
abline(v=1/154, lty = "dotted")
abline(v=1/30, lty = "dotted")
# spectral density of deep volcanic earthquake
va.sp <- spectrum(va.ts, spans = c(5,7), taper =0.1,log = "yes", main = "Deep
    Volcanic Earthquake", sub= "Cycles/day, smoothed" )
va.sp$freq[which.max(va.sp$spec)] # to reveal the frequency domain of the
    highest spectrum
frequency(va.ts)/(va.sp$freq[which.max(va.sp$spec)]) # to reveal the period of
    the highest spectrum
abline(v=0.004340278, lty = "dotted")
# spectral density of shallow volcanic earthquake
vb.sp <- spectrum(vb.ts, spans = c(5,7), log = "yes", main = "Shallow Volcanic
    Earthquake", sub= "Cycles/day, smoothed" )
vb.sp$freq[which.max(vb.sp$spec)] # to reveal the frequency domain of the
    highest spectrum
frequency(vb.ts)/(vb.sp$freq[which.max(vb.sp$spec)]) # to reveal the period of
    the highest spectrum

abline(v=0.00390625, lty = "dotted")
```

Cross Correlation Analysis

Cross Correlation Seismic Features Data

```
### loading the seismic dataset
sve=read.csv("Volcanic and tectonic earthquake.csv", header=T)
### convert to time series
## Local tectonic
tl.ts <- ts(sve$TL, start=c(2008,1), frequency = 365 )
plot(tl.ts)
library(xts)
```

```
tl.xts=xts(sve$TL, as.Date(sve$Date, format = '%m/%d/%y'))
plot(tl.xts)
## Deep volcanic
va.ts <- ts(sve$VA, start=c(2008,1), frequency = 365 )
plot(va.ts)
va.xts=xts(sve$VA, as.Date(sve$Date, format = '%m/%d/%y'))
plot(va.xts)
## Shallow volcanic
vb.ts <- ts(seismic$VB, start=c(2008,1), frequency = 365 )
plot(vb.ts)
vb.xts=xts(sve$VB, as.Date(sve$Date, format = '%m/%d/%y'))
plot(vb.xts)
### Correlation
## correlation Local tectonic and Deep of Volcanic Earthquake
tl.va.interst <- ts.intersect(tl.ts, va.ts)
plot(tl.va.interst, plot.type = "single", main = "Local Tectonic and Deep VT")
lines(lowess(tl.ts, f = 1/3), col = "red")
lines(lowess(va.ts, f = 1/3), col = "blue")
plot(tl.va.interst, plot.type = "multiple", main = "Local Tectonic and Deep
    Volcanic Earthquake")
cc.tl.va <- ccf(tl.ts, va.ts, main="Cross correlation between Local Tectonic and
    Deep Volcanic Earthquake")
max(abs(cc.tl.va$acf))
(i <- which.max(abs(cc.tl.va$acf)))
cc.tl.va$acf[i]
12 * cc.tl.va$lag[i]
### correlation Local tectonic and shallow of Volcanic Earthquake
tl.vb.interst <- ts.intersect(tl, vb)
plot(tl.vb.interst, plot.type = "single", main = "Local Tectonic and Shallow
    Volcanic Earthquake")
lines(lowess(tl, f = 1/3), col = "red")
lines(lowess(vb, f = 1/3), col = "blue")
plot(tl.vb.interst, plot.type = "multiple", main = "Local Tectonic and Shallow
    Volcanic Earthquake")
cc.tl.vb <- ccf(tl, vb, main="Cross correlation between Local Tectonic and
    Shallow Volcanic Earthquake")
cc.tl.vb
max(abs(cc.tl.vb$acf))
(i <- which.max(abs(cc.tl.vb$acf)))
cc.tl.vb$acf[i]
12 * cc.tl.vb$lag[i]
```

Cross correlation Short-Term Time Siries Data between seismic and CO_2 dataset

```
## Loading dataset of seismic and CO2 gas of 2011toxic gases outburst event
dieng <- read.csv("Time series 2011.csv", header=T)
## convert to time series format
# Time series of maximum CO2 emissions
co2.max.txt=xts(dieng$CO2.max, as.Date(dieng$Date, format = '%m/%d/%y'))
co2.max.ts <- zoo(dieng$CO2.max, order.by=as.Date(as.character(dieng$Date),
      format ='%m/%d/%y'))
plot(cd01.max.zoo, type = "l", pch = 20, cex=0.6, main = "Time Series of
      Maximum Carbon Dioxide of 2011 event",
   ylab = " Frequences")
co2.av.ts <- ts(dieng$CO2.max, start=c(2011,4), frequency=365)
# local tectonic seismic
tl.xts=xts(dieng$TL, as.Date(dieng$Date, format = '%m/%d/%y'))
plot(tl.xts, main="Local Tectonic Earthquake")
tl.zoo<- zoo(dieng$TL, order.by=as.Date(as.character(dieng$Date), format
      ='%m/%d/%y'))
plot(tl, type = "l", pch = 20, cex=0.6, main = "Time Series of Local Tectonic
      Earthquake", ylab = " Frequences")
tl.ts <- ts(dieng$TL, start=c(2011,4,4), frequency=365)
# deep volcanic seismic
va.xts=xts(dieng$VA, as.Date(dieng$Date, format = '%m/%d/%y'))
plot(va.xts, main="Deep Volcanic Earthquake")
va.zoo <- zoo(dieng$VA, order.by=as.Date(as.character(dieng$Date), format
      ='%m/%d/%y'))
va.ts <- ts(dieng$VA, start=c(2011,4), frequency=365)
plot(va.ts)
# shallow volcanic seismic
vb.xts=xts(dieng$VB, as.Date(dieng$Date, format = '%m/%d/%y'))
plot(vb.xts, main="Shallow Volcanic Earthquake")
vb.zoo <- zoo(dieng$VB, order.by=as.Date(as.character(dieng$Date), format
      ='%m/%d/%y'))
vb.ts <- ts(dieng$VB, start=c(2011,4), frequency=365)
plot(vb.ts)
## Local tectonic seismic with CO2 emissions
# local tectonic seismic with maximum CO2 emission
tl.co2.max <- ts.intersect(tl.ts, co2.max.ts)
plot(tl.co2.max, plot.type = "multiple", main = "Tectonic local seismic and
      Maximum CO2 Emissions")
(ccf(tl.zoo, co2.max.zoo, main = "Cross correlation between Tectonic local
      seismic and Maximum CO2 emission"))
## Depth volcanic seismic with CO2 emissions
# cross correlation with maximum CO2
va.co2.max <- ts.intersect(va.ts, co2.max.ts)
```

```
plot(va.co2.max, plot.type = "multiple", main = "Depth Volcanic Earthquake and
    Maximum CO2")
(ccf(va.zoo, co2.max.zoo, main = "Cross correlation between Depth volcanic
    Earthquake and Maximum CO2 emission"))
## Shallow volcanic seismic with CO2 emissions
#### cross correlation with maximum CO2
vb.co2.max <- ts.intersect(vb.ts, co2.max.ts)
plot(vb.co2.max, plot.type = "multiple", main = "Shallow Volcanic Earthquake
    and Maximum CO2")
(ccf(vb.zoo, co2.max.zoo, main = "Cross correlation between Shallow volcanic
    Earthquake and Maximum CO2 emission"))
```

Plot Earthquake Magnitude and Energy

```
En13 <- read.csv("Volcanic and tectonic energy.csv")
en <- En13
library(lubridate)
En13$Date <- mdy_hm(En13$Date)
library(ggplot2)
qplot(Date, M, data=En13, shape= Type, color=Type, ylab="Magnitude")
qplot(Date, Energy, data=En13,shape= Type, color=Type, ylab="Earthquake
    Energy")
```